

An exploratory study on the aerosol height retrieval from OMI measurements of the 477 nm O₂–O₂ spectral band, using a Neural Network approach

Julien Chimot¹, J. Pepijn Veeffkind^{1,2}, Tim Vlemmix¹, Johan F. de Haan², Vassilis Amiridis³, Emmanouil Proestakis^{3,4}, Eleni Marinou^{3,5}, and Pieter Felicitas Levelt^{1,2}

¹Department of Geoscience and Remote Sensing (GRS), Civil Engineering and Geosciences, TU Delft, the Netherlands

²Royal Netherlands Meteorological Institute, De Bilt, the Netherlands

³Institute for Astronomy, Astrophysics, Space Applications and Remote Sensing, National Observatory of Athens, Athens 15236, Greece

⁴Laboratory of Atmospheric Physics, Department of Physics, University of Patras, 26500, Greece

⁵Department of Physics, Aristotle University of Thessaloniki, Thessaloniki, 54124, Greece

Correspondence to: J. Chimot (j.j.chimot@tudelft.nl)

Abstract. This paper presents an exploratory study on the aerosol layer height (ALH) retrieval from the OMI 477 nm O₂–O₂ spectral band. We have developed algorithms based on the Multilayer Perceptron (MLP) Neural Network (NN) approach and applied them on 3-year (2005-2007) OMI cloud-free scenes over North-East Asia, collocated with MODIS-Aqua aerosol product. In addition to the importance of aerosol altitude for climate and air quality objectives, our long-term motivation is to evaluate the possibility of retrieving ALH for potential future improvements of trace gas retrievals (e.g. NO₂, HCHO, SO₂, etc..) from UV-Vis air quality satellite measurements over scenes including high aerosol concentrations. This study presents a first step of this long-term objective and evaluates, from a statistic point-of-view, an ensemble of OMI ALH retrievals over a long-time period of 3 years covering a large industrialized continental region. This ALH retrieval relies on the analysis of the O₂–O₂ slant column density (SCD) and requires an accurate knowledge of the aerosol optical thickness τ . Using MODIS-Aqua $\tau(550\text{nm})$ as a prior information, absolute seasonal differences between the Lidar climatology of vertical Aerosol Structure for space-based lidar simulation (LIVAS) and average OMI ALH, over scenes with MODIS $\tau(550\text{nm}) \geq 1.0$, are in the range of 260-800 m (assuming single scattering albedo $\omega_0 = 0.95$) and 180-310 m (assuming $\omega_0 = 0.9$). OMI ALH retrievals depend on the assumed aerosol single scattering albedo (sensitivity up to 660 m) and the chosen surface albedo (variation less than 200 m between OMLER and MODIS Black Sky albedo). Scenes with $\tau \leq 0.5$ are expected to show too large biases due to the little impacts of particles on the O₂–O₂ SCD changes. In addition, NN algorithms also enable aerosol optical thickness retrieval by exploring the OMI reflectance in the continuum. Comparisons with collocated MODIS-Aqua show agreements between -0.02 ± 0.45 and -0.18 ± 0.24 depending on the season. Improvements may be obtained from a better knowledge of the surface albedo, and higher accuracy of the aerosol model. Following the previous work over ocean of Park et al. (2016), our study shows the first encouraging aerosol layer height retrieval results over land from satellite observations of the 477 nm O₂–O₂ absorption spectral band.

1 Introduction

The ability to monitor air quality and climate from UltraViolet-Visible (UV-Vis) satellite spectral measurements requires accurate trace gas (e.g. NO_2 , SO_2 , HCHO, O_3) and aerosol observations. Aerosols and trace gases often share similar anthropogenic sources, and their concentrations, as shown by the satellite observations, often exhibit significant correlations (Veeffkind et al., 2011). The reason is that trace gases are often precursors for aerosols. The importance of measuring vertical distribution of atmospheric aerosols on a global scale is triple. Firstly, aerosols directly impact the radiation budget of the Earth-atmosphere system through the scattering and absorption of solar and terrestrial radiation (Feingold et al., 1999). High concentrations of fine particles lead to reduced cloud droplet size, enhanced cloud reflectance (Twomey et al., 1984), and reduced precipitation (Rosenfeld, 2000; Ramanathan et al., 2001; Rosenfeld et al., 2002). Therefore, large uncertainties of aerosol optical properties limit our climate predictive capabilities (IPCC: Solomon et al., 2007). In spite of more robust climate predictions in the last years, radiative forcing (RF) induced by aerosols are still the largest uncertainty to the total RF estimate (IPCC: The Core Writing Team Pachauri and Meyer, 2014). The vertical distribution and relative location are determining factors of aerosol radiative forcing in the long-wave spectral range (Dufresne et al., 2002; Kaufman et al., 2002). Secondly, aerosols play a significant role in air quality, in particular near the surface. Due to the rapid growth of both population and economic activity, such as in Asian region, increase in fossil fuel emissions gives rise to concerns about fine particles formation and dispersion. Aerosols include a variety of hazardous organic and inorganic substances, reduce visibility, lead to reductions in crop productivity and strongly affect health of inhabitants in urban regions (Chameides et al., 1999; Prospero, 1999; Eck et al., 2005).

Thirdly, slant column densities (SCD) of trace gases, derived from UV-Vis air quality space-borne sensors, have a high sensitivity to aerosol heights. For partly cloudy conditions, clouds are the main error source of trace gas measurements. But, in the absence of clouds, vertical distribution of aerosols, combined with their scattering and absorbing properties, modifies the length of the average light path of the detected photons, and therefore affects trace gas Air Mass Factors (AMF). The application of the AMF is crucial for the conversion of slant column densities (SCD) from satellite line-of-sight measurements into vertical column densities. Then, aerosols strongly contribute to the uncertainties of trace gas retrievals from space-borne observations. For example, the magnitude of the error on the Ozone Monitoring Instrument (OMI) tropospheric NO_2 retrieval is, over polluted areas, mostly determined by the AMF uncertainty, not by the SCD uncertainty. It results from the combination of aerosols, clouds and the shape of the NO_2 profile (Boersma et al., 2007). Negative biases on OMI tropospheric NO_2 columns, between -26% and -50% , are found in urban and very polluted areas in cases of high aerosol pollution and particles located at elevated altitude (Shaiganfar et al., 2011; Ma et al., 2013; Kanaya et al., 2014). HCHO AMF for GOME-2 and SCanning Imaging Absorption spectroMeter for Atmospheric CHartographY (SCIAMACHY) shows about 20-50% sensitivity to aerosols, depending whether they are located within or above the boundary layer (Barkley et al., 2012; Hewson et al., 2015). Dust aerosols (large particles, with strong absorption in UV) can reduce the AMF in the SO_2 wavelengths (310 - 330 nm) by half, thus doubling the retrieved SO_2 (Krotkov et al., 2008). This impacts the ability of sensors like OMI to monitor Planetary Boundary Layer (PBL) SO_2 with a sensitivity to local anthropogenic sources. Over regions of enhanced

columns, aerosols highly contribute to the total SO_2 AMF error (Lee et al., 2009). Therefore, aerosol parameters (or retrievals) are a pre-requisite before retrieving trace gas vertical column densities.

State-of-the-art trace gas retrieval algorithms correct for aerosol effects either explicitly using modeled aerosol vertical profiles (e.g., (Barkley et al., 2012, 2013; Kuhlmann et al., 2015; Lin et al., 2014, 2015)), or alternatively implicitly via cloud algorithms. For example, the OMI $\text{O}_2\text{--O}_2$ absorption band at 477 nm has been widely exploited to derive cloud information (Acarreta et al., 2004; Sneep et al., 2008). However, the OMI cloud algorithm is sensitive to aerosols, and thus the retrieved effective cloud parameters are modified in their presence (Boersma et al., 2007; Castellanos et al., 2015; Chimot et al., 2016). The OMI $\text{O}_2\text{--O}_2$ spectral band at 477 nm contains significant information on aerosol properties and height. The retrieved effective clouds are then used to correct the computed AMF (de Smedt et al., 2008; Boersma et al., 2011). In spite of these well considered perturbations, the use of the effective cloud parameters, assuming that the opaque Lambertian cloud model can reproduce the distribution of scattering fine particle effects, does not yet completely correct for the aerosol effects when computing the AMF, in particular for the tropospheric NO_2 columns (Castellanos et al., 2015; Chimot et al., 2016).

Characterizing the aerosol vertical distribution, in addition to the associated optical properties, using passive space-borne measurements is challenging due to the absence of spectral features in the aerosol optical properties and the combined influences of surface and cloud reflection. Contrary to effective cloud retrievals, aerosol retrieval is a more complex problem mainly because of the variability of particle microphysical properties and the lower optical thickness (typically 1-2 orders of magnitude). As a consequence, methods assuming large multiple scattering contributions, such as a simple cloud model with Lambertian properties, cannot be used. Passive radiometers like Moderate Resolution Imaging Spectroradiometer (MODIS) can only retrieve a limited amount of independent information from their measurements, usually aerosol optical thickness τ and the extinction Ångström exponent α , as a proxy for the particle size distribution (Levy et al., 2007, 2013). The near-UV technique has been widely used to map the daily global distribution of UV-absorbing aerosols such as desert dust particles as well as carbonaceous aerosols generated by anthropogenic biomass burning and wildfires. It allows to retrieve τ , Single Scattering Albedo ω_0 and the qualitative Aerosol Absorbing Index (AAI) in the 330-388 nm of the Total Ozone Mapping Spectrometer (TOMS) and OMI sensors (Torres et al., 1998; Torres et al., 2002; Torres et al., 2007). However, this technique is highly affected by the dependency of the measured radiances on the height of the absorbing aerosol layer (Torres et al., 1998; de Graaf et al., 2005). OMAERUV has been upgraded by integrating a monthly climatology of CALIOP aerosol heights to retrieve aerosol parameters from OMI UV measurements (Torres et al., 2013). The Cloud-Aerosol Lidar with Orthogonal Polarization (CALIOP) has been providing vertical profiles of aerosols but with limited spatial coverage because of its measurements characteristics (Omar et al., 2009). Park et al. (2016) evaluated the sensitivity of the $\text{O}_2\text{--O}_2$ slant column density to changes in aerosol layer height over ocean. It is demonstrated that the $\text{O}_2\text{--O}_2$ spectral band at 477 nm is the most sensitive to the aerosol layer effective height (compared to the $\text{O}_2\text{--O}_2$ absorption bands at 340, 360 and 380 nm), due to the largest $\text{O}_2\text{--O}_2$ absorption and reduced Rayleigh scattering. Veihelmann et al. (2007) determined that the complete OMI UV-Vis reflectance measurements contain between 2 and 4 Degrees of Freedom of Signal (DFS). The 477 nm $\text{O}_2\text{--O}_2$ band adds by itself about 1 degree and therefore contains more information than any other individual band. This relative large number of DFS for UV-Vis satellite solar backscatter observations is explained by the sensitivity of the reflectance to the aerosol layer

height. Detailed O_2-O_2 radiative transfer simulations performed by Dirksen et al. (2009) revealed the availability of the altitude information about smoke aerosol plume, released by intense forest fires and transported over long distance, under specific conditions: high AAI and no clouds. In spite of all these efforts, no aerosol height retrieval has been done at this moment from O_2-O_2 satellite measurements at 477 nm over land.

5 Since aerosol altitude, in addition to τ , is one of the key parameters affecting the computation of AMF for trace gases retrievals such as NO_2 (Leitão et al., 2010; Chimot et al., 2016), our long-term motivation is to evaluate the capability of retrieving it from the satellite O_2-O_2 absorption band at 477 nm. This exploratory study is the first step and statistically analyses an ensemble of OMI observations over a three year period (from 2005 to 2007) and covering a large industrialized continental region (i.e. North-East Asia). This study follows the conclusions of previous works focused on the sensitivity of
10 this spectral band and the observed links between the O_2-O_2 effective cloud retrievals and aerosol parameters. In this paper, quite a few algorithm concepts are developed, based on the Neural Network (NN) approach, and then tested on a high number of OMI observations over land. Our primary focus is the retrieval performance of aerosol layer pressure (ALP) associated with scattering and fine particles over large urban, industrialized and highly polluted area and cloud-free scenes. In addition, the sensitivity of the algorithms to τ knowledge is investigated and, therefore, the capability of τ retrievals from the same OMI band
15 is evaluated. The considered satellite observations and input dataset are described in Sect. 2. Sect. 3 focuses on the available OMI O_2-O_2 Differential Optical Absorption Spectroscopy (DOAS) parameters and their link with Aerosol Layer Height (ALH) and τ . The development of the different NN algorithms are described in Sect. 4. Their performances are evaluated in Sect. 5 on synthetic and independent data set with a characterization of the main limiting factors. Finally, these algorithms are applied in Sect. 6 to cloud-free OMI observation over the North-East Asia where large amounts of aerosols are emitted from
20 both natural and anthropogenic sources (Lee et al., 2012). They are then compared with other observation products, namely MODIS Aqua τ and the Lidar climatology of vertical Aerosol Structure for space-based lidar simulation (LIVAS).

2 Aerosol and surface albedo satellite data

In this section, are described the three main aerosol satellite data that are used in this study: OMI Visible measurements, MODIS aerosol product and LIVAS climatology database. In addition, the two considered surface albedo databases: OMI
25 Lambert Equivalent Spectral Surface Reflectance (OMLER) and MODIS Black Sky Albedo are also detailed.

2.1 OMI satellite data

The Dutch-Finnish mission OMI (Levelt et al., 2006) is a nadir-viewing push-broom imaging spectrometer launched on the National Aeronautics and Space Administration (NASA) Earth Observing System (EOS)-Aura satellite. It provides daily global coverage of key air quality components through observations of the backscattered solar radiation that are captured in the UV-
30 Vis spectral domain. Based on a two-dimensional detector array concept, radiance spectra are simultaneously measured on a 2600 km wide swath within a nadir pixel size of $13 \times 24 \text{ km}^2$ ($28 \times 150 \text{ km}^2$ at extreme off-nadir). OMI has a higher spatial

resolution than any other UV-Vis hyperspectral spectrometers. It measures in the wavelength range of 270 nm to 500 nm with a spectral resolution of 0.45 nm in the UV-2 band (310-360 nm) and 0.63 nm in the visible band (360-500 nm).

Starting mid-2007, the so-called "row anomaly" has been perturbing OMI measurements of the Earth-shine radiance at all the wavelengths. Details are given on the site <http://www.knmi.nl/omi/research/product/rowanomaly-background.php>. For practical reasons, this study only used the OMI data acquired during 2005-2007, i.e. before the development of this anomaly.

OMI has not been optimized for aerosol monitoring. However, the OMI near-UV aerosol algorithm (OMAERUV) independently retrieves atmospheric total columns of τ and ω_0 from the 2 UV wavelengths, 354 nm and 388 nm (Torres et al., 2007, 2013). In comparison with 44 Aerosol Robotics Network (AERONET) sites, evaluated OMAERUV τ yield a root mean square error (RMSE) of 0.16 and a correlation coefficient of 0.81 over the years 2005-2008 (Ahn et al., 2014). About 65 % of these retrievals lie within the expected uncertainty. The OMAERUV ω_0 product agrees with AERONET to within 0.03 in 46,% of the collocated pairs, and to within 0.05 in 69 % of the cases (Jethva et al., 2014).

The OMI O₂-O₂ 477 nm absorption band is currently operationally exploited by the OMI O₂-O₂ cloud algorithm to derive effective cloud fraction and pressure (Acarreta et al., 2004; Veeffkind et al., 2016). Park et al. (2016) applied a Look-Up-Table (LUT) approach on this band to retrieve aerosol effective height over ocean, close to East Asia, within the error range of 1 km (compared to CALIOP). This approach was applied to 7 case studies, each of them covering a few days. No τ was retrieved. No study has yet explicitly used this satellite band to directly retrieve ALH and τ over land. This band is not only available on OMI but also on various sensors such GOME-2, OMPS and the next Tropospheric Ozone Monitoring (TROPOMI) space-borne.

2.2 MODIS aerosol product

The MODIS instrument, launched on the NASA EOS-Aqua platform in May 2002, is a spectrometer delivering continuous images of the Earth in the visible, solar and thermal infrared approximately 15 min prior to OMI on-board EOS-Aura. The considered MODIS Aqua Level 2 (L2) aerosol product is the collection 6 of *MYD04_L2*, based on the Dark Target (DT) Land algorithm with a high enough quality flag (Xiao et al., 2016). While the MODIS measurement is acquired at the resolution of 1 km, the MODIS aerosol product is available at both 3 km x 3 km and 10 km x 10 km. Since this last one is relatively close to the OMI nadir spatial resolution, it is then used in the work below (c.f. Sect. 7). The improved calibration of MODIS Aqua instrument is included in the reprocessing of the collection 6 aerosol product (Levy et al., 2013; Lyapustin et al., 2014).

The availability of the MODIS aerosol products is generally a good confirmation of cloud-free scenes as MODIS Aqua τ variable is exclusively given provided a high amount of cloud-free sub-pixels is available (i.e. the MODIS measurement resolution of 1 km).

The expected error of MODIS DT τ is about $\pm 0.05 + 15\%$ over land (Levy et al., 2013). The "Deep Blue" retrieval algorithm has been developed to complement the DT algorithm by retrieving τ over bright arid land surfaces (e.g. deserts). The typical associated uncertainties are about ± 0.03 on average (Sayer et al., 2013).

2.3 LIVAS climatology database

The Lidar climatology of Vertical Aerosol Structure for space-based lidar simulation studies (LIVAS) is a 3-D multi-wavelength global aerosol and cloud optical database (Amiridis et al., 2015). This database provides averaged profiles of aerosol optical properties over 9 years (1 January 2007 - 31 December 2015) from the Cloud Aerosol Lidar and Infrared Pathfinder Satellite Observations (CALIPSO) data on a uniform grid of $1^\circ \times 1^\circ$. LIVAS addresses the wavelength dependency of aerosol properties for many laser operating wavelengths including 532 nm. LIVAS data set has been evaluated against AERONET in Amiridis et al. (2015) showing realistic and representative mean state aerosol optical depth values in 532 nm making this data set ideal for synergistic use with other satellite products.

The LIVAS ALH is derived from the given averaged vertical profile of aerosol extinction (532 nm) $\sigma(l)$ over each vertical layer l defined by its altitude $h(l)$ as follow:

$$ALH(LIVAS) = \frac{\sum_1 h(l)\sigma(l)}{\sum_1 \sigma(l)} \quad (1)$$

Since LIVAS also provides the standard deviation associated with each averaged vertical profile of aerosol extinction (532 nm) $\partial\sigma(l)$, the equivalent standard deviation ∂ALH of each LIVAS ALH is derived as follow:

$$\partial ALH(LIVAS) = \frac{\sum_1 \partial h(l)\partial\sigma(l)}{\sum_1 \sigma(l)} \quad (2)$$

where $\partial h(l)$ is the geometric thickness of each vertical layer l .

2.4 Surface albedo dataset

The standard and reference surface albedo product is the OMLER climatology derived from several years of OMI observations at the spatial resolution of $0.5^\circ \times 0.5^\circ$ longitude-latitude grid for each calendar month (Kleipool et al., 2008). The OMLER algorithm is based on temporal histograms of the observed Lambert Equivalent Spectral Surface Reflectance (LER) values per grid box. Potential small residual cloud and aerosol contaminations are expected to remain in the OMLER product. As an alternative, the global and spatially complete MODIS black sky surface albedo in the band 3 (459-479 nm) is considered. It is defined as the directional hemispherical reflectance and is a function of solar zenith angle θ_0 (Schaaf et al., 2002). It is derived by integrating the atmospheric corrected Bidirectional Reflectance Distribution Function (BRDF), derived from combined MODIS-Aqua and Terra observations over every 16-day period. The downwelling flux in the MODIS Black Sky albedo has no diffuse component. The Collection 6 of MCD43C3 product is given on a 0.05° (5.6 km) latitude/longitude Climate Modeling Grid (CMG). Note that (Kleipool et al., 2008) demonstrated that the OMLER data set is closer to the black sky than to the white sky by evaluating the ratio between diffuse and direct illumination.

3 OMI O₂–O₂ DOAS analysis and aerosols

3.1 DOAS analysis of the OMI O₂–O₂ 477 nm absorption band

In this paper, the aerosol Neural Network (NN) retrieval algorithms allow the conversion of the continuum reflectance $R_c(475\text{nm})$ and the O₂–O₂ SCD $N_{\text{O}_2-\text{O}_2}^s$ into $\tau(550\text{nm})$ and ALP (in hPa). As a consequence, the NN retrievals rely on the way how the aerosol parameters modify these two variables and thus the photons average light path.

Prior to this conversion, a spectral DOAS fit must be performed to derive $R_c(475\text{nm})$ and $N_{\text{O}_2-\text{O}_2}^s$ from the OMI O₂–O₂ 477 nm absorption band. The various DOAS techniques rely on the same key concept: a simultaneous fit of several trace gas slant column densities from the fine spectral features due to their absorption (i.e. the high frequency part) present in passive UV-Vis spectral measurements of atmospheric radiation (Platt and Stutz, 2008). Here, the DOAS fit follows the same approach as in the OMI O₂–O₂ cloud algorithm (Acarreta et al., 2004; Veeffkind et al., 2016): i.e. the absorption cross-section spectrum of O₂–O₂ is fitted together with a first order polynomial:

$$-\ln(R(\lambda)) = \gamma_1 + \gamma_2 \cdot \lambda + N_{\text{O}_2-\text{O}_2}^s(\lambda) \cdot \sigma_{\text{O}_2-\text{O}_2} + N_{\text{O}_3}^s(\lambda) \cdot \sigma_{\text{O}_3}, \quad (3)$$

where $\gamma_1 + \gamma_2 \cdot \lambda$ defines the first order polynomial, $\sigma_{\text{O}_2-\text{O}_2}$ and σ_{O_3} are the O₂–O₂ and O₃ absorption cross-section spectra respectively, convoluted with the OMI slit function, and $N_{\text{O}_3}^s$ is the O₃ slant column density. $\sigma_{\text{O}_2-\text{O}_2}$ is based on measurements of the cross section made by C. Hermans (see <http://www.aeronomie.be/spectrolab/o2.htm> - file O4.txt). The O₃ cross section spectrum is included because it overlaps with the O₂–O₂ spectrum. The fitted parameters are γ_1 , γ_2 , $N_{\text{O}_2-\text{O}_2}^s$, and $N_{\text{O}_3}^s$. In the absence of absorbers, one may define the continuum reflectance R_c at the reference wavelength λ_0 :

$$R_c = \exp(-\gamma_1 - \gamma_2 \cdot \lambda_0). \quad (4)$$

The reference wavelength is specified as the middle of the DOAS fit window at $\lambda_0 = 475$ nm.

3.2 On the impact of aerosols on R_c and O₂–O₂ SCD

Figure 1 illustrates how aerosol particles directly drive the OMI O₂–O₂ DOAS parameters at 477 nm assuming cloud-free space-borne observations. These effects are obtained from radiative transfer simulations including aerosols and no clouds. The detailed generation of such simulations is given in Sect. 4.2. The DOAS fit equations following Eq. (3) and Eq. (4) are then applied to these simulations. In this paper, the aerosol layer is assumed to be one single scattering layer (i.e. "box layer") with a constant geometric thickness (about 1 km). All the particles included in this layer are supposed to be homogeneous (i.e. same size and optical properties). ALH is then expressed by ALP, in hPa, defined as the mid-pressure of this scattering layer.

Qualitatively, aerosols have two separate effects on the average light path, and therefore on the O₂–O₂ absorption signal at the top of the atmosphere (TOA). These two effects are similar to aerosols and clouds have on NO₂ absorption signal (Leitão et al., 2010; Chimot et al., 2016): 1) a shielding effect, i.e. a decreased sensitivity within and below the aerosol layer due to a reduced amount of photons coming from the TOA and reaching the lowest part of the atmosphere compared to an aerosol-free scene, 2) an enhancement (albedo) effect, i.e. an increased sensitivity within and above the aerosol layer as

more photons are scattered back towards the sensors, the part of the atmosphere above the aerosol layer is then sampled by a larger fraction of detected photons. Shielding then leads to a reduced O_2-O_2 absorption while enhancement may increase the O_2-O_2 absorption especially for low cloud or aerosol layers. The overall effect (enhancement vs. shielding) depends on the aerosol optical properties, the total column τ and ALP.

5 OMI $R_c(475\text{nm})$ is directly and primarily affected by the total column τ of particles present in the observed scene. Indeed, R_c increases with increasing τ independently of the ALP (cf. Fig. 1a). This mostly results from the influence of aerosols on the number of detected photons and on the additional scattering effects observed in the scene compared to an aerosol-free scene. However, the magnitude of this increase relies on aerosol optical properties and the surface brightness. As a consequence, R_c is also affected by aerosol ω_0 , phase function, and the surface albedo A . Indeed, R_c decreases with decreasing ω_0 and over a
 10 darker surface (i.e. smaller A value) for all the τ values (cf. Fig. 1c and Fig. 1e). The importance of these parameters is further discussed in Sect. 5 and Sect. 6. Note that, in addition, the reflectance is also driven by the geometry angles: i.e. viewing zenith angles θ , θ_0 and relative azimuth angle defined as the difference between viewing and zenith azimuth angles $\phi - \phi_0$. An increase of θ or θ_0 will lead to longer average light path, and thus will amplify aerosol related additional scattering effects (for a given τ).

15 OMI $N_{O_2-O_2}^s$ relies on the O_2-O_2 absorption magnitude along the average light path in the whole atmosphere. It is driven by the overall shielding or enhancement effect of photons by the O_2-O_2 complex in the visible spectral range, due to the presence of particles. As depicted in Fig. 1b, $N_{O_2-O_2}^s$ decreases with decreasing ALP. This is a direct consequence of a larger shielding effect applied by aerosols located at higher altitudes (i.e. part of the O_2-O_2 complex located below the aerosol layers are shielded). Nevertheless, in case of low τ values (i.e. ≤ 0.5), $N_{O_2-O_2}^s$ does not significantly vary with respect to ALP. This
 20 shows that a low amount of aerosols has very little impacts on O_2-O_2 absorption measurements.

However, as depicted in Fig. 1b, 1d and 1f, not only ALP but also τ directly influences the slant O_2-O_2 absorption since both parameters simultaneously affect the average path followed by the photons, and therefore the overall shielding or enhancement effect. At a given altitude, an increase of τ leads to a decrease of $N_{O_2-O_2}^s$. The slope of this decrease depends on the aerosol altitude (i.e. higher for particles at high altitude). Note that both ω_0 and A also affect $N_{O_2-O_2}^s$, but this effect is
 25 smaller than τ . For example, a reduced ω_0 and A lead to a small decrease of $N_{O_2-O_2}^s$ (cf. Fig. 1d and Fig. 1f).

As a consequence:

- the single parameter $N_{O_2-O_2}^s$ contains information on both τ and ALP. These parameters cannot be separated from this unique variable alone. Therefore, if τ is not accurately known, there will likely be an ambiguity when analysing $N_{O_2-O_2}^s$ to retrieve ALP.
- 30 – if an external or prior τ estimate is not available, then the two parameters $N_{O_2-O_2}^s$ and $R_c(475\text{nm})$ could be simultaneously and directly combined to retrieve ALP provided that one can accurately and independently retrieve τ from $R_c(475\text{nm})$. Then, in that condition, OMI $R_c(475\text{nm})$ may help to distinguish both τ and ALP contributions in $N_{O_2-O_2}^s$. However, the simultaneous effects of aerosol ω_0 and A on R_c (as discussed above), and therefore their associated un-

certainties, will impact the feasibility of retrieving τ from OMI measurements. It may then degrade the retrieved ALP performances.

- τ , R_c and $N_{\text{O}_2-\text{O}_2}^s$ have a non negligible correlation. Indeed, an increase of τ results in a simultaneous increase of R_c and $N_{\text{O}_2-\text{O}_2}^s$. Therefore, it has to be noted that these two last parameters are not independent and combining them does not provide with two independent pieces of information.

Overall, the impact of aerosol particles on the OMI O_2-O_2 spectral band is similar to cloud particles. This explains in part the difficulty to distinguish aerosols from clouds. In cases with a mix of aerosols and clouds, there is an ambiguity between R_c , τ and the OMI effective cloud fraction on the one hand, and $N_{\text{O}_2-\text{O}_2}^s$, ALP, τ , the OMI effective cloud pressure and fraction on the other hand (Boersma et al., 2011; Castellanos et al., 2015; Chimot et al., 2016). Therefore, this study only focuses on cloud-free reflectance to avoid this complexity.

4 Design of the neural network retrieval algorithms

The retrieval algorithms developed for this paper are based on the Pybrain software (Schaul et al., 2010). Pybrain is a versatile machine learning library written in Python designed to facilitate both the application of and research on premier learning algorithms such as recurrent NNs. It includes several functions such as supervised learning algorithms, feed forward network design and error back-propagation computations. Only the main developments specific to the present study are explained and discussed in the next sub-sections. For more details related to the Pybrain specificities, the reader is encouraged to read Schaul et al. (2010).

The Multilayer Perceptron (MLP) neural networks have been widely used and acknowledged for decades in the field of remote sensing (Atkinson and Tatnall, 1997). Indeed, most retrieval problems in this field are ill-posed and nonlinear. Thus, the associated inverse problems can only be addressed by including a priori information and relying on statistical analysis. Since aerosol retrieval from passive spectral measurements is well-known as a non-linear inverse problem, the MLP technique represents then a powerful approach to design a retrieval algorithm in a fast and robust way. The basic idea is to build an optimal interpolator system making the link between OMI 477 nm O_2-O_2 measurements and the retrieved ALP and $\tau(550\text{nm})$ (cf. Fig. 1). However, knowledge must be acquired by the NNs by means of a supervision database. The following sections summarize then the design of the developed algorithms (see Sect. 4.1), the generated supervision database (see Sect. 4.2) and the employed learning process (Sect. 4.3).

4.1 Multilayer Perceptron network approach: application to the OMI O_2-O_2 aerosol retrievals

Artificial NNs are a family of models related to the machine learning and the artificial intelligence domain (Luger and Stubblefield, 1998). They are used to reduce the number of calculations of functions requiring a large number of inputs and being generally unknown (or not well defined). The idea is to approximate them by parameterized and more simple functions. Input and output signals are then interconnected by a set of activation functions and a set of weights associated with each of them

(Luger and Stubblefield, 1998). In the context of this work, no invertible analytical function exist that describes the dependence of slant columns and continuum reflectances on aerosols (see Sect. 2.3). Thus, the idea of developing neural networks here is to identify input-output relationships directly from a well-known training ensemble. The choice of a NN approach relies on their advantages compared to more conventional methods such as linear regression, linear interpolation in a LUT or the

5 Optimal Estimation Method (OEM). In particular, it enables 1) very fast computations with modern computers in spite of the number of required parameters, 2) optimized interpolation technique even in case of non-linear statistical modelling and so, potentially, lower systematic biases compared to a linear interpolation, 3) reduced memory use compared to a LUT with a very high sampling.

As illustrated in Fig. 2, the designed NNs rely on a multi-layer architecture, based on the Multilayer Perceptron technique, composed of parallel processors (i.e. neurons) organized in distinct layers (Rumelhart et al., 1986). Such an architecture allows to separate non-linear data, and generally consists of 3 (or more) types of layers. The first layer includes all the required input variables. The last layer includes all the desired output data (or here retrievals). The intermediate layers are usually referred as hidden layers and contain the activation functions. All these layers are connected via neural links: two nodes or neurons i and j between two consecutive layers have synaptic connections associated with a synaptic weight ω_{ij} . Each neuron j computes

15 a weighted sum of its N x_i information sent from the neurons of previous layer (cf. Eq. (6)). Then, this weighted sum is transported through a non-linear mathematical function before being passed to the next layer (cf. Eq. (5) and Eq. (6)). Here use is made of the classical sigmoid function:

$$\sigma(x) = \frac{1}{1 + \exp(-x)}. \quad (5)$$

The output z_j of the neuron j in the hidden layer is thus given by:

$$20 \quad z_j = \sigma\left(\sum_{i=1}^N \omega_{ij} \cdot x_i\right). \quad (6)$$

The overall set W of synaptic weights ω_{ij} contain all the information about the network (i.e. its neural architecture defined by a specified number of layers, neurons and connections). When the transport reaches the output layer, it forms the network output.

The chosen neural architecture is the following (see Fig. 2). The input layer is composed of 7 parameters that include (1) θ ,

25 θ_0 , $\phi - \phi_0$, surface pressure Ps , surface albedo A , and (2):

- either $R_c(475\text{nm})$ and $N_{\text{O}_2-\text{O}_2}^s$ for $\tau(550\text{nm})$ and ALP retrievals: this configuration is named $NN_{R_c, N_{\text{O}_2-\text{O}_2}^s}$,
- or $\tau(550\text{nm})$ and $N_{\text{O}_2-\text{O}_2}^s$ for ALP retrieval: this configuration is named $NN_{\tau, N_{\text{O}_2-\text{O}_2}^s}$.

The output layer is, for each NN retrieval algorithm, composed of only one output variable: either $\tau(550\text{nm})$, or ALP . In total, three NN retrieval algorithm configurations are then selected and used at the end: one $NN_{R_c, N_{\text{O}_2-\text{O}_2}^s}$ for $\tau(550\text{nm})$ retrieval,

30 one $NN_{R_c, N_{\text{O}_2-\text{O}_2}^s}$ and one $NN_{\tau, N_{\text{O}_2-\text{O}_2}^s}$ for ALP retrieval.

The choice to use either $NN_{R_c, N_{\text{O}_2-\text{O}_2}^s}$ or $NN_{\tau, N_{\text{O}_2-\text{O}_2}^s}$ will impact the accuracy of the ALP retrieval results (see Sect. 5.2 and 5.3).

4.2 Generation of the supervision database: aerosol properties and simulations

The MLP neural networks must be accurately trained from a well-known data set. They are then able to generalize the inverse problem by predicting the aerosol retrievals from input observations that have never been seen before. For that purpose, a learning database must be carefully designed and generated. It must be representative of the entire distribution of (input-output) values that can likely be encountered in the OMI observations. As a consequence for the MLP algorithms, a large quantity of data is often required for the learning process. However, very large learning data set can be extremely time consuming in terms of generation and then NN training.

Training a neural network based on a large ensemble of synthetic dataset has been widely employed in atmospheric retrieval science such as for CO₂ and CH₄ (Crevoisier et al., 2009a, b), aerosol (Di Noia et al., 2015) and cloud properties (Loyola, 2004; Loyola et al., 2007, 2010). This study created our own training dataset based on simulations from the Determining Instrument Specifications and Analyzing Methods for Atmospheric Retrieval (DISAMAR) software of KNMI (de Haan, 2011). DISAMAR includes a radiative transfer model and different retrieval methods. The radiative transfer model is based on the Doubling Adding KNMI (DAK) model (de Haan et al., 1987; Stammes, 2001) and thus computes the reflectance and transmittance in the atmosphere using the adding/doubling method. This method calculates the internal radiation field in the atmosphere at levels to be specified by the user and takes into account Rayleigh, aerosol and cloud scattering and trace gas and aerosol absorption. Scattering by aerosols is simulated with a Henyey–Greenstein scattering phase function $\Phi(\Theta)$ (Hovenier and Hage, 1989):

$$\Phi(\Theta) = \frac{1 - g^2}{(1 + g^2 - 2g \cos \Theta)^{3/2}}. \quad (7)$$

where Θ is the scattering angle. The phase function is then parameterized by the asymmetry parameter g , which is the average of the cosine of the scattering angle, such its variation $-1 \leq g \leq 1$ ranges from back-scattering through isotropic scattering to forward scattering. Following the DISAMAR configuration, τ values in the simulations are specified at the reference wavelength of 550 nm. The Ångström exponent α describes the spectral dependence of τ .

ALP is the main target parameter since this is one of the main parameters describing the average light path distribution in the tropospheric NO₂ AMF computation. The second target is $\tau(550\text{nm})$ since this information may be requested for a good ALP retrieval quality. We thus assume we do not need at this level to define more realistic aerosol models for every aerosol scene. With a reference asymmetry parameter of $g = 0.7$, intermediate value typically observed (Dubovik et al., 2002), the Henyey–Greenstein function is known to be smooth and reasonably well reproduce the Mie scattering functions for most of aerosol types. This approach is also used for the preparation of the operational aerosol layer height retrieval algorithm from Sentinel-5 Precursor (Sanders et al., 2015) and for explicit aerosol corrections in the AMF calculation when retrieving trace gases such as tropospheric NO₂ (Spada et al., 2006; Wagner et al., 2007; Castellanos et al., 2015).

The ensemble of parameters and associated values used for generating the learning database is detailed in Table 1. About 460 000 spectral simulations, over the O₂–O₂ spectral band (460–490 nm), were generated, assuming different satellite viewing and solar geometries, A , Ps and aerosol pollution levels. Scenes with too large angles (i.e. $\theta_0 \geq 65^\circ$) and too bright surfaces (i.e. $A > 0.1$) are excluded. For each of these simulations, $R_c(475\text{nm})$ and $N_{\text{O}_2-\text{O}_2}^s$ were deduced from the DOAS fit equations

Eq. (3) and Eq. (4). Aerosols are specified for a standard case, assuming fine particles with a unique value of $\alpha = 1.5$ and $g = 0.7$. Aerosol profiles are parameterized by scattering layers with constant aerosol volume extinction coefficient and ω_0 and with a fixed pressure thickness. In order to investigate the assumptions related to the single scattering albedo properties ω_0 , two typical values are considered: $\omega_0 = 0.95$ and 0.9 . Contrary to the other variables, ω_0 is not known for each OMI pixel and thus cannot be used as an explicit input parameter by the designed NNs. Moreover, it cannot be retrieved from this band since it is supposed to affect $R_c(475\text{nm})$ and $N_{\text{O}_2-\text{O}_2}^s$, similarly as τ . Therefore, 2 sets of NN models are developed for different purposes:

- one set of three MLP NN algorithms ($NN_{R_c, N_{\text{O}_2-\text{O}_2}^s}$ for $\tau(550\text{nm})$ retrieval, $NN_{R_c, N_{\text{O}_2-\text{O}_2}^s}$ and $NN_{\tau, N_{\text{O}_2-\text{O}_2}^s}$ for ALP retrieval) is trained with a learning database including aerosol spectral simulations assuming $\omega_0 = 0.95$;
- one set of three MLP NN algorithms ($NN_{R_c, N_{\text{O}_2-\text{O}_2}^s}$ for $\tau(550\text{nm})$ retrieval, $NN_{R_c, N_{\text{O}_2-\text{O}_2}^s}$ and $NN_{\tau, N_{\text{O}_2-\text{O}_2}^s}$ for ALP retrieval) is trained with a learning database including aerosol spectral simulations assuming $\omega_0 = 0.9$.

The choice to use one of these sets will impact the accuracy of the retrieval results.

4.3 Optimization of the learning process and selection of the best NN architecture

Prediction of the optimal NN architecture (i.e. number of neurons and hidden layers) is generally not possible as these values are strongly specific to the given problem (Atkinson and Tatnall, 1997). While it has been theoretically proven that a single hidden layer MLP networks with non-linear activation functions may represent any nonlinear continuous function (Haykin, 1999), a 2-hidden layer MPL may approximate any function to any degree of non-linearity taking also into account discontinuities (Sontag, 1992). To identify the best NN architecture for each aerosol retrieval parameter (τ and ALP) and for each configuration ($NN_{R_c, N_{\text{O}_2-\text{O}_2}^s}$ or $NN_{\tau, N_{\text{O}_2-\text{O}_2}^s}$, see Sect. 3.1), several architectures are trained and then evaluated: one single hidden layer with a variable number of neurons (between 9 and 70) and two hidden layers (between 15 and 70 neurons on the 1st layer, and between 10 and 40 on the 2nd layer). Then, the optimal NN architecture is selected based on the best computed evaluation score. In total, about 96 different MLP architectures, for each configuration, were evaluated.

For one given NN architecture, the training process is the optimization technique that estimates the optimal network parameters W of synaptic weights σ_{ij} (see Sect. 3.1). For that purpose, an error function E must be minimized. This error function measures, for a set of p representative situations, for which inputs and outputs (i.e. $\tau(550\text{nm})$ and ALP) are known, the mismatch between the neural network outputs o_i and the true outputs t_i as follow:

$$E = \frac{1}{2} \sum_{i=1}^p (o_i - t_i)^2. \quad (8)$$

This error function minimization follows here the Error Back-Propagation algorithm as specified by Rumelhart et al. (1986). It is a stochastic steepest descent algorithm well adapted to the MLP hierarchical architecture. The learning step is made sample by sample, iteratively and stochastically selected in the training data set. The network is initialized with random synaptic weights. At each iteration, the error is computed and then propagated backwards from the output layer. The processes of error

back-propagating and feeding forward signals are repeated iteratively until the error function is minimized or the maximum number of iterations is reached (i.e. 500).

During the training phase, the considered network architecture must obtain an optimal generalization performance: i.e. the network performance should not degrade significantly when data set other than the training one is analyzed. Standard NN architectures, like the fully connected MLP, generally have a too large parameter space, and are prone to over-fitting. Although the network performance seems to constantly improve on the training sets at each iteration, it can actually begin to worsen (in terms of errors) on unseen data set. Therefore, a verification step is performed, over the last 15 iterations, to detect this overfitting moment (i.e. no significant variation of E) and stop the training phase. This process is called early stopping. Finally, to ensure that the system is not trapped in local minima during the error function minimization, the learning phase (training+verification) is repeated three times, the synaptic weights being randomly initialized at the beginning of each training phase. The network system presenting the best evaluation score (see Eq. 8) is then selected. All these precautions are carried out by randomly splitting the learning data (see Table 1) into 3 independent sets: training, verification and evaluation. They respectively consisted of 70 %, 15 % and 15 %.

Figure 3 depicts the box-whisker plots of the square of errors obtained over the ensemble of training-verification-evaluation data set for $\tau(550\text{nm})$ and ALP retrieval and for $NN_{R_c, N_{\text{O}_2-\text{O}_2}^s}$ configuration, assuming $\omega_0 = 0.95$. For $\tau(550\text{nm})$ retrievals, although the NNs with 40 and 70 neurons on one hidden layer do reasonably well, the scores show improved values when two hidden layers are used. The ALP retrieval scores are significantly larger than for τ (a factor of 100). This is a direct consequence that ALP is less well constrained by the spectral measurements: lower pieces information are available compared to τ , in particular for scenes dominated by low τ values. While the NNs with one hidden layer do not show any significant improvements when increasing number of neurons, better scores are only obtained with 2 hidden layers. Overall, the similar behavior of training-verification-evaluation scores validate that the trained NNs are generalized enough to be able to reproduce similar variation of the scores on other independent data set. The identified best NN algorithms are thus found with 2 hidden layers, including between 25 and 70 neurons on the first layer, and between 10 and 20 neurons on the second layer depending on the considered configuration and retrieved parameter (see Sect. 2.3).

5 Sensitivity analyses on synthetic data set

The robustness of the trained and selected NN retrieval algorithms is assessed by applying them to independent simulations, not present in the learning (training-verification-evaluation) database. Simulated spectra are noise-free and only include aerosol particles (no clouds). The sensitivity of $\tau(550\text{nm})$ and ALP retrievals is verified for different A and aerosol properties (ω_0 , τ , ALP). $R_c(475\text{nm})$ and $N_{\text{O}_2-\text{O}_2}^s$ are derived from the spectra and provided as inputs to the NNs. The impact of uncertainties on surface albedo, aerosol model and $N_{\text{O}_2-\text{O}_2}^s$ are analysed. Consistent geophysical conditions (temperature, NO_2 and O_3 profiles) are considered between these simulations and those included in the learning database. All the analyses performed here are summarized in Table 2.

5.1 Aerosol Optical Thickness retrievals

Figure 4 compares the retrieved to the true $\tau(550\text{nm})$ values of the simulated spectra, and how uncertainties on ω_0 , g and A degrade the retrieval quality. Overall, retrieved and true $\tau(550\text{nm})$ values are very well correlated for all the types of surface, assuming no error in the assumed surface albedo and aerosol properties. This confirms the success of the learning process implemented in Sect. 4.2 and Sect. 4.3 and the use of the NN approach.

The assumed aerosol properties (ω_0 and phase function through g), and so the choice of the trained NN algorithm, are of high importance. They change the slope between retrieved and true τ values and drastically affect the retrieved $\tau(550\text{nm})$ accuracy. If the assumed ω_0 (i.e. 0.95) through the simulations in the learning database is too high (true $\omega_0 = 0.9$), retrieved τ is then underestimated: i.e. a bias of -0.8 for $\tau(550\text{nm}) = 2$, and -0.1 for $\tau(550\text{nm}) \leq 0.5$ (see Fig. 4a). This is a direct consequence of reduced scattering efficiency as more photons are absorbed instead of being scattered back towards the satellite sensor. The measured $R_c(475\text{nm})$ is then lower (cf. Fig. 1). Reciprocally, an assumed too low aerosol ω_0 (i.e. true $\omega_0 = 1.0$) leads to an overestimation of retrieved $\tau(550\text{nm})$: i.e. a bias of 1.0 for $\tau(550\text{nm}) = 2$ (cf. Fig. 4a).

Figure 4b illustrates retrieved $\tau(550\text{nm})$ bias due to the difference between the assumed g in the learning database and in the synthetic spectra. While $g = 0.7$ is the reference value for most of aerosols, scenes with $g = 0.6$ are related to finer and weakly absorbing particles with a somewhat reduced forward scattering direction such as carbonaceous aerosols, desert dust and volcanic ash models as given by the ESA aerosol CCI-project (de Leeuw et al., 2013). Values of $g = 0.8$ are associated with larger particles and an increased forward scattering direction such as cirrus (Sanders et al., 2015). An overestimation of g (i.e. assumed $g = 0.7$ while true $g = 0.6$) leads to an increased retrieved τ value (i.e. positive bias) because of less photons scattered towards the surface, and therefore more photons scattered back towards the satellite sensor, compared to what is theoretically assumed. Reciprocally, an underestimation of g (i.e. assumed $g = 0.7$ while true $g = 0.8$) leads to a decreased retrieved τ value (i.e. negative bias) due to less photons scattered back towards the satellite sensor, and more towards the surface compared to the assumption. Absolute bias values can exceed 0.5 for $\tau(550\text{nm}) = 1.5$ while they stay close to 0.25 for $\tau(550\text{nm}) = 0.5$.

Errors in surface albedo also lead to biases in retrieved $\tau(550\text{nm})$ (cf. Fig. 4c). Overall, biases are larger over scenes with small $\tau(550\text{nm})$ values. The reason is the dominance of surface reflection in this regime. Only in cases of high amount of aerosols, then aerosol scattering signals become dominant and surface reflection uncertainties have less impacts. An underestimated (overestimated) surface albedo results in a negative (positive) retrieved $\tau(550\text{nm})$ bias. This is directly related to the change in the measured OMI R_c (cf. Fig. 1). Surface albedo uncertainties in the range of 0.025-0.05 lead to absolute biases close to 0.5 for $\tau(550\text{nm})$ in the range of 0.0-0.5, smaller than 0.25 for $\tau(550\text{nm}) = 2.0$. Typical differences in climatological surface albedo from the total ozone monitoring spectrometer (TOMS) and the global ozone monitoring experiment (GOME) (Koelemeijer et al., 2003), or between OMLER and the MODIS black sky albedo (Kleipool et al., 2008), are known to be up to 0.02.

5.2 Aerosol Layer Pressure retrievals

Figure 5 and Figure 6 depict the expected performances of the developed NN algorithms for ALP retrievals. Over scenes with $\tau(550\text{nm})$ in the range of 0.5-1.0, and assuming no error in prior A and the employed aerosol model, ALP retrievals are relatively stable presenting biases close to 100 hPa. Only for $\tau(550\text{nm}) \geq 1.0$, biases are smaller than 50 hPa. The accuracy of the retrieved ALP generally increases with increasing τ . Indeed, assuming true ALP of 850 hPa (see Fig. 6), positive biases larger than 400 hPa are found for $\tau(550\text{nm}) \leq 0.5$. Note that this behavior is observed for all the NN configurations ($NN_{R_c, N_{\text{O}_2-\text{O}_2}^s}$ and $NN_{\tau, N_{\text{O}_2-\text{O}_2}^s}$). A box-whisker plot, in Figure 7, illustrates the variability of the ALP NN biases as a function of $\tau(550\text{nm})$ over all the simulations contained in the entire learning database (as defined and used in Sect.3). This confirms that, in spite of the strict training-verification-evaluation process achieved in Sect. 4.3, the NN ALP retrievals are not expected to be accurate for small $\tau(550\text{nm})$ values, especially below 0.5. The reason is directly linked to the magnitude of the O_2-O_2 shielding effect and its combined dependence on aerosol amount (or τ) and aerosol altitude (cf. Fig. 1 and Sect. 3.2). Because low amount of aerosols have very limited effects on the O_2-O_2 absorption (see Sect. 3.2), even advanced interpolation techniques like NNs have difficulties to interpret the associated signal. When τ increases, the O_2-O_2 shielding effect amplifies and the algorithms are more able to link the O_2-O_2 absorption signal to ALP. Overall, even for small $\tau(550\text{nm})$ values (like 0.5), the retrieved aerosol pressures correlate with the true values in spite of very poor accuracy (see Fig. 6a and Fig. 6c).

A very accurate prior τ information as input is required to generally improve the ALP retrieval performances. As explained in Sect. 3.2, using $NN_{R_c, N_{\text{O}_2-\text{O}_2}^s}$ implicitly relies on the $\tau(550\text{nm})$ retrieval capability from OMI $Rc(475\text{nm})$. Using $NN_{\tau, N_{\text{O}_2-\text{O}_2}^s}$ with the true $\tau(550\text{nm})$ value as input (thus no error) is expected to deliver higher performances. Firstly, it allows to improve the accuracy of the ALP retrieval over scenes with low τ and particles located at high altitude (above 800 hPa or 2 km). Indeed, in Fig. 5b, for $\tau(550\text{nm}) = 0.5$ and ALP between 750 and 850 hPa, ALP biases are reduced from 250-350 hPa with $NN_{R_c, N_{\text{O}_2-\text{O}_2}^s}$ to 150-250 hPa with $NN_{\tau, N_{\text{O}_2-\text{O}_2}^s}$ and true $\tau(550\text{nm})$ value. For particles higher than 650 hPa (or 3.5 km), no improvements are however observed. The low sensitivity to retrieve ALP when particles are located at a very high altitude is directly due to the O_2-O_2 complex and its vertical distribution. This was demonstrated by Park et al. (2016): O_2-O_2 concentration exponentially decreases with increasing atmospheric altitude.

Secondly, impacts due to uncertainties on the chosen surface albedo and aerosol model are reduced. Assumptions on aerosol ω_0 drive the interpretation of the shielding of the O_2-O_2 dimers by aerosols. ω_0 can perturb ALP retrievals obtained with $NN_{R_c, N_{\text{O}_2-\text{O}_2}^s}$ more than 100 hPa (see Fig. 5a). These perturbations are reduced to the range of 0-100 hPa over scenes with high $\tau(550\text{nm})$ values (larger than 1) only for particles close to the surface, i.e. true $ALP \geq 850\text{hPa}$ (see Fig. 6a and Fig. 6c). Using $NN_{\tau, N_{\text{O}_2-\text{O}_2}^s}$ with true $\tau(550\text{nm})$ value helps to mitigate these biases. All the ALP retrievals present the same behaviours with respect to the particles altitude and τ and biases lie in the range of 0-50 hPa (see Fig. 5b). Similar conclusions are observed regarding uncertainties on g (cf. Fig. 5c and Fig. 5d). Too high g values impact the ALP retrievals from $NN_{R_c, N_{\text{O}_2-\text{O}_2}^s}$ over scenes with $\tau(550\text{nm}) \leq 1.0$. Such a bias is largely reduced with the $NN_{\tau, N_{\text{O}_2-\text{O}_2}^s}$ configuration.

Surface albedo contributes to the length of the average light path and thus affects $N_{\text{O}_2-\text{O}_2}^s$. Retrieved ALP biases are maximum (several hundreds hPa) for $\tau(550\text{nm}) \leq 0.5$ (cf. Fig. 8a and Fig.8b). For $\tau(550\text{nm})$ in the range of 0.5-1.0, retrieved

ALP are impacted by lower absolute values (between 50 hPa and 100 hPa on average) with $NN_{\tau, N_{O_2-O_2}^s}$, while they remain too high with $NN_{R_c, N_{O_2-O_2}^s}$. Over scenes with $\tau(550\text{nm}) \geq 1.0$, biases are reduced to 0-50 hPa since aerosol scattering signals dominate over surface reflection. The main cause of all these improvements is that using an accurate prior τ information (or at least more than retrieved OMI $\tau(550\text{nm})$ from $R_c(475\text{nm})$) allows a better distinction of τ and ALP effects on the

5 O_2-O_2 slant column density and reduce impacts of A and ω_0 uncertainties.

An accuracy better than 0.2 must be required on prior τ information (cf. Fig. 8c). Indeed, a $\tau(550\text{nm})$ bias of 0.25 can impact, in absolute, the retrieved ALP up to 50 hPa for $\tau(550\text{nm})$ in the range of 0.6-1.0. For $\tau(550\text{nm}) \geq 1.0$, impact on ALP becomes almost null. Therefore, using MODIS τ as prior to $NN_{\tau, N_{O_2-O_2}^s}$ is likely expected to show retrieved ALP with a higher quality than with $NN_{R_c, N_{O_2-O_2}^s}$. Indeed, the current retrieved OMI $\tau(550\text{nm})$ from $R_c(475\text{nm})$ does not present a

10 better accuracy than MODIS $\tau(550\text{nm})$.

Figure 9 depicts the box-whisker distribution of ALP precision $\epsilon(\partial N_{O_2-O_2}^s)$ due to $N_{O_2-O_2}^s$ precision. Estimations are obtained for fine and scattering particles ($\alpha = 1.5$, $\omega_0 = 0.95$, $g = 0.7$). $\epsilon(\partial N_{O_2-O_2}^s)$ is obtained from the half of ALP differences between adding and deducting uncertainties of the variables as follows:

$$\epsilon(\partial N_{O_2-O_2}^s) = \frac{1}{2} |ALP(N_{O_2-O_2}^s + \partial N_{O_2-O_2}^s) - ALP(N_{O_2-O_2}^s - \partial N_{O_2-O_2}^s)|. \quad (9)$$

15 where $\partial N_{O_2-O_2}^s$ is the uncertainty applied to $N_{O_2-O_2}^s$. $\epsilon(\partial N_{O_2-O_2}^s)$ values are computed for all combinations of surface albedo 0.03-0.05-0.07 and $\theta_0-\theta = [25^\circ-25^\circ, 50^\circ-25^\circ, 25^\circ-45^\circ]$. The reason to use this approach here is that, since $N_{O_2-O_2}^s$ precision is a random error (opposite to systematic), it will directly impact the retrieved ALP precision instead of leading to a systematic bias. A precision of $N_{O_2-O_2}^s$ lying in the range of $0.05-0.25 \cdot 10^{-43} \text{ mol}^2\text{cm}^{-5}$ (i.e. at a first order, 2-7 % of $N_{O_2-O_2}^s$) results in ALP uncertainties between 19 ± 29 hPa and 57 ± 31 hPa on average for both NN configurations (see

20 Fig. 5c).

Overall all the estimated NN retrieval uncertainties are in line with the theoretical sensitivity analyses of Park et al. (2016) who found that the O_2-O_2 at 477 nm is significantly influenced by aerosol optical properties (including ω_0), τ , particle size and A . In particular, a ω_0 uncertainty of 10 % was demonstrated to lead to the aerosol effective height (AEH) retrieval error ranging from 270 to 1440 m, depending on the aerosol types. Errors were found larger for high particle altitude and low τ

25 cases. A surface albedo uncertainty of 0.02 was expected to impact AEH retrievals between 154 m and 434 m on average. AEH error was frequently larger only for low $\tau(550\text{nm}) (\leq 0.4)$ and high AEH (≥ 1 km).

6 Application to OMI observation measurements

6.1 Methodology

Aerosol retrievals, as described in the previous sections, are performed on the OMI O_2-O_2 477 nm observations over large

30 industrialized continental areas in North-East Asia over 3 years, 2005-2007, and cloud-free scenes. All the associated results are summarized in Table 2. The considered North-East Asia area is defined by the range of latitude $25-40^\circ$ North, and longitude $110-130^\circ$ East excluding the part over the Gobi desert which presents a too bright surface (as further explained below).

Only OMI observations collocated with MODIS Aqua L2 aerosol product collection 6 are considered (cf. Sect. 2.2). The reason is triple: 1) to maximize the probability of the selection of cloud-free OMI observation pixels dominated by aerosol pollution, 2) to evaluate the retrieved OMI $\tau(550\text{nm})$ products by comparing with collocated MODIS $\tau(550\text{nm})$, 3) to use the MODIS $\tau(550\text{nm})$ as input of the $NN_{\tau, N_{\text{O}_2-\text{O}_2}^s}$ algorithm for retrieving the OMI ALP product, assuming then this is the most accurate τ information available for each collocated OMI observation pixel-MODIS aerosol grid cell.

MODIS data are paired on a OMI pixel-by-pixel basis if the distance between OMI pixel center and MODIS aerosol grid cell is smaller than 5 km and if both observation and product are acquired within 15 min. A threshold of 0.1 is applied to both OMI and MODIS cloud fraction: i.e. if the OMI effective cloud fraction and/or the MODIS geometric cloud fraction (given in the same MODIS aerosol product at 10 km resolution) has a cloud fraction value higher than 0.1, the OMI pixels are filtered out. However, since the OMI effective cloud fraction is sensitive to the scattering aerosols, it is well recognized that cloud-free observations with large presence of scattering aerosols are frequently excluded as well. In addition, a threshold of 0.1 is applied to the OMLER database in order to filter out too bright surfaces (either desert or snow covered pixels).

The NN retrieval algorithms developed and selected in Sect. 3 are used and evaluated here: $NN_{R_c, N_{\text{O}_2-\text{O}_2}^s}$ for $\tau(550\text{nm})$ and ALP retrievals, $NN_{\tau, N_{\text{O}_2-\text{O}_2}^s}$ with MODIS $\tau(550\text{nm})$, from DT algorithm over land, as input for ALP retrieval. For reminder, retrieving ALP from $NN_{R_c, N_{\text{O}_2-\text{O}_2}^s}$ is implicitly similar than from $NN_{\tau, N_{\text{O}_2-\text{O}_2}^s}$ but with the retrieved OMI $\tau(550\text{nm})$, as input (cf. Sect. 3.2 and 5.2). All the NNs designed and trained with the two different ω_0 (i.e. 0.9 and 0.95) are considered in order to investigate the impact of ω_0 assumptions.

These algorithms are applied on the OMI DOAS O_2-O_2 observations, available in the OMCLDO2 product (Acarreta et al., 2004) which can be downloaded here: http://disc.sci.gsfc.nasa.gov/Aura/data-holdings/OMI/omcldo2_v003.shtml. As explained in Veefkind et al. (2016), $N_{\text{O}_2-\text{O}_2}^s$ depends on the temperature profile due to the nature of dimers of which the absorption scales with the pressure-squared instead of being linear with pressure. Therefore, a simple temperature correction is here applied by using seasonal mean temperature profiles given by the National Centers for Environmental Prediction (NCEP) analysis data. This correction is performed through the computation of the γ factor (Veefkind et al., 2016):

$$\gamma = \frac{N_{\text{O}_2-\text{O}_2}^{\text{sRef}}(\lambda)}{N_{\text{O}_2-\text{O}_2}^{\text{sMeas}}(\lambda)}. \quad (10)$$

with $N_{\text{O}_2-\text{O}_2}^{\text{sRef}}$, the O_2-O_2 SCD associated with the reference temperature profile employed in the learning database and $N_{\text{O}_2-\text{O}_2}^{\text{sMeas}}$, the measured O_2-O_2 SCD related to the actual temperature conditions. As a first and simple approximation, no prior knowledge on aerosols is considered here. The main reason is the little sensitivity to aerosol loading and altitude of this γ factor, for $\tau(550\text{nm}) \leq 2.0$, compared to the change of temperature profiles for the considered OMI observations.

Finally, retrievals are performed based on different assumed surface albedo databases: either OMLER or MODIS Black Sky Albedo (cf. Sect. 2.4). The MODIS Black Sky Albedo is resampled to match the OMI pixel resolution by calculating the average of all MODIS pixels falling within the processed OMI pixel.

6.2 Aerosol optical thickness accuracy: on the importance of the surface albedo and the assumed aerosol properties

Figure 10 compares collocated retrieved OMI and MODIS $\tau(550 \text{ nm})$. Similarly to the analyses on synthetic cases (cf. Sect. 5.1), the change of assumed ω_0 , mostly perturbs retrievals of high τ values, and thus the slope between OMI and MODIS $\tau(550 \text{ nm})$. Increasing ω_0 from 0.9 to 0.95 reduces the retrieved τ values of about 0.5 for MODIS $\tau = 1.5$. Overall a very
5 good agreement is obtained assuming $\omega_0 = 0.9$ for the seasons spring, autumn and winter (see Fig. 10 and Fig. 13): differences (OMI-MODIS) of $\tau(550 \text{ nm})$ lie between -0.18 ± 0.24 in winter and -0.02 ± 0.45 in spring. In summer time, the best agreements are found assuming $\omega_0 = 0.95$ with differences in the range of -0.06 ± 0.31 (see Fig. 8 and Fig. 12).

From the end of autumn to spring, westerly winds transport mineral dust from the Taklimakan and Gobi deserts in northern China and Mongolia region. These dust particles are then frequently mixed with the local anthropogenic aerosols released from
10 the industrial activities, vehicle emissions and coal burning (Eck et al., 2005). Southeast Asia is affected in spring by biomass-burning activity (mostly over the peninsular) which is a major source of carbonaceous aerosols in the world. Jethva et al. (2014) show that AERONET and OMAERUV retrieve aerosol ω_0 values on average between 0.9 and 0.95 in these regions: most of the sulphate particles have ω_0 close to 0.95, while smoke and dust present lower values (closer to 0.9, even below in some cases). These analysis confirm that the assumption of $\omega_0 = 0.95$ should be considered as an upper limit for the OMI τ
15 retrievals in autumn, winter and spring times, while a lower ω_0 (i.e. 0.9) is likely more appropriate and thus allows, on average, more reliable τ retrievals. In summer time, because of reduced amounts of dust particles, τ values are more representative of local anthropogenic urban pollution, with a higher daily variability in the optical and scattering properties. Lee et al. (2007); Lin et al. (2015) also found higher ω_0 values over North-East Asia in summer (0.95-0.96) and lower for the other seasons (0.88-0.92). Overall, assuming same constant value (i.e. average) for all the acquired OMI pixels probably lead to some errors
20 since aerosol scattering and absorption properties likely vary day-to-day, even month-to-month.

Figure 11 depicts the dependence of the retrieved OMI $\tau(550\text{nm})$ on the OMLER surface albedo values. As discussed in Sect. 5.1, error in surface albedo directly creates a bias on the retrieved τ . Most of the retrievals depict higher values over darker surfaces, or lower surface albedo. In the range of OMI surface albedo values 0.05-0.1, such behavior should not be observed assuming no systematic bias on the surface properties. Moreover, OMI $\tau(550\text{nm})$ shows too small values for scenes
25 with MODIS $\tau(550\text{nm}) \leq 0.4$ in autumn and winter using OMLER (see Fig. 11 and Fig. 14). MODIS Black Sky surface albedo allows to reduce this dependence in summer and spring and reasonably increases OMI τ retrievals over scenes with low MODIS τ values in autumn and winter (cf. Fig. 14). Furthermore, standard deviation of differences (OMI-MODIS) $\tau(550 \text{ nm})$ shows a net improvement of the retrievals precision, with a mean reduction of 0.05 from OMLER to MODIS Black Sky (cf. Fig. 12). An exception is however noticed in winter, which may be due to remaining snow covered pixels in spite of the applied
30 filtering. Overall, spatial patterns better match between collocated MODIS and OMI products when employing MODIS Black Sky albedo with higher values over the high density population areas (i.e. North-East and South-West of selected Chinese region, South-West of Korea) and lower values over South-East of China (see Fig. 13 and Fig. 14). These improvements may be due to a more accurate atmospheric correction in the MODIS Black Sky surface albedo and potential remaining aerosol residuals present in the OMLER database.

In spite of these improved precisions, using the MODIS Black Sky albedo does not always improve the accuracy of the OMI $\tau(550\text{nm})$ retrievals. In particular, summer and spring seasons present too high τ values compared to the use of OMLER. This emphasizes that applying the MODIS Black Sky albedo to OMI measurements may be not fully optimal as: 1) MODIS albedo is the integral value over the full hemisphere which is not in line with the range of angles (θ_0 and θ) encountered by OMI, 2) the MODIS Black Sky albedo is valid for local solar noon zenith angle of each location which does not match the 1345 ascending node equator crossing time of OMI. An ideal surface albedo database should be aerosol and cloud free, and representative of the viewing and solar angles encountered by the space-borne sensor. Problems related to uncertainties in surface albedo climatology for the aerosol retrieval problem are well known, and has recently been highlighted by Sanders et al. (2015), although a different spectral band is used (O_2-A at 758-770 nm).

As a conclusion, mostly because uncertainties on assumed aerosol ω_0 parameter and prior surface albedo are dominant, our retrieved OMI $\tau(550\text{nm})$ show lower performances than MODIS $\tau(550\text{nm})$ from the DT algorithm over land in Collection 6 (cf. Sect. 2.2). Furthermore, errors in the phase function or not taking into account the effect of polarization, can play a role. These aspects should be further investigated.

6.3 Long-term analyses of the aerosol layer pressure retrievals

Figure 15 shows the retrieved OMI ALP as a function of collocated MODIS $\tau(550\text{ nm})$. MODIS $\tau(550\text{nm})$ is considered for OMI ALP retrievals since, at this stage, they are considered as the best prior information available with higher accuracy than OMI $\tau(550\text{nm})$ (cf, Sect. 6.1). While ALP retrievals over scenes with MODIS $\tau(550\text{nm}) \leq 0.5$ exhibit large variability (more than 400 hPa) and are systematically very high, they start converging to more realistic values with increasing MODIS τ . At MODIS $\tau(550\text{nm}) \geq 1.0$, retrieved ALP lies in the range of 800-1000 hPa depending on the season, with lower variability (between 50 hPa and 200 hPa maximum). As discussed in Sect. 5.2, scenes with $\tau \leq 0.5$ are expected to present substantial large biases because of the minor impacts on the O_2-O_2 changes. Part of the variability can be related to uncertainties of surface albedo and non-constant and inhomogeneous aerosol properties from OMI pixel-to-pixel (e.g. aerosol ω_0 in the OMI observations).

When considering $NN_{\tau, N_{O_2-O_2}^s}$ with MODIS $\tau(550\text{ nm})$, from DT algorithm over land, as input, the retrievals globally show a reduced variability, especially for $\tau(550\text{nm})$ values in the range of 0.6-2.0 compared to the $NN_{R_c, N_{O_2-O_2}^s}$ configuration (see Fig. 16). Over scenes with MODIS $\tau(550\text{nm}) \geq 1.0$, the variability of the OMI ALH, derived from Eq. 11 as explained in the next subsection, greatly decreases from the range of 1.1-2.7 km ($NN_{R_c, N_{O_2-O_2}^s}$) to 0.7-1.9 km ($NN_{\tau, N_{O_2-O_2}^s}$) depending on the season. When the OMLER is replaced by the MODIS Black Sky albedo database, the ALH variability continues to decrease of about 0.1 km (cf. Fig. 16).

6.4 Comparison of OMI aerosol layer height with LIVAS climatology

The results of 3 years of OMI ALP retrievals over North-East Asia can be statistically compared to a climatology. Although the years of the OMI "climatology" and LIVAS do not strictly overlap, the average ALH is assumed not to change significantly between both periods. The comparison is done per season. Spatial average of LIVAS ALH is done over the same area where

retrievals are performed. Since large biases are expected at low τ , only OMI retrievals acquired for MODIS $\tau(550\text{nm}) \geq 1.0$ are taken into account and then spatially and temporally averaged per season. About 17 % in summer and spring, and between 5 % and 6 % in winter and autumn, of the OMI retrievals over the 3 years were then selected. As a first and simple approximation, OMI ALP retrievals are converted into ALH in km above sea level, assuming the atmosphere is in hydrostatic balance, scale height of 8 km and a surface pressure at the sea level of 1013 hpa:

$$ALH(OMI) = -8 * \ln(ALP/1013). \quad (11)$$

Assumptions on the forward aerosol model (used then in the creation of the supervision database) lead to the highest impacts on the spatial-seasonal averaged ALH retrievals. This is mostly related to the ability of the corresponding NN algorithm to interpret the scattering vs. absorption aerosol effects on the $N_{O_2-O_2}^s$. Assuming OMLER surface albedo, differences between average ALH retrievals with $\omega_0 = 0.95$ and $\omega_0 = 0.9$ are in the range of 540-1200 m with $NN_{R_c, N_{O_2-O_2}^s}$, and 560-660 m with $NN_{\tau, N_{O_2-O_2}^s}$ using MODIS $\tau(550\text{nm})$. Assumptions on prior surface albedo (OMLER vs. MODIS Black Sky Albedo) also affect the spatial-seasonal averaged ALH retrievals. Related differences are in the range of 0-730 m with $NN_{R_c, N_{O_2-O_2}^s}$, and 0-180 m with $NN_{\tau, N_{O_2-O_2}^s}$. Note that a remarkable change is noticed using MODIS Black Sky Albedo in winter with $NN_{R_c, N_{O_2-O_2}^s}$ which is likely due to non-filtered snow covered pixels. Associated impacts are then lower than those related to assumed ω_0 . Since only scenes with MODIS $\tau(550\text{nm}) \geq 1.0$ are selected, aerosol scattering signal is expected to dominate over the surface brightness. Although not shown here, we remarked that applying the temperature correction on $N_{O_2-O_2}^s$ is crucial as it corrects the retrievals between 50 m and 300 m.

Because MODIS $\tau(550 \text{ nm})$ has a better accuracy than OMI $\tau(550 \text{ nm})$, seasonal-spatial average ALH retrievals from $NN_{\tau, N_{O_2-O_2}^s}$ combined with this first product shows a clear reduced impact and higher stability with respect to uncertainties on surface albedo and aerosol model. This is because using the most accurate prior information on aerosol amount provides then with the best ALH retrieval performance.

By comparing these best ALH results with the seasonal spatial averaged LIVAS ALH values, maximum differences in the range of 260-800 m are obtained, depending on the seasons, assuming $\omega_0 = 0.95$ and OMLER surface albedo. These differences are reduced to 180-310 m with $\omega_0 = 0.9$ regardless the prior surface albedo. Furthermore, when comparing with the LIVAS ALH variability (cf. Eq. 2) spatially averaged over the area, the results from $NN_{\tau, N_{O_2-O_2}^s}$ with MODIS $\tau(550 \text{ nm})$ and prior MODIS Black Sky albedo have the closest variability with a spread in the range of 0.0-1.0 km (cf. Fig. 16).

Consistent seasonal patterns can be observed between averaged OMI and LIVAS ALH with higher values in spring and summer, probably due to long-range transport during the dust activity from the desert (cf. Sect. 6.2) and smaller values in autumn and winter (cf. Fig. 17). Nevertheless, while the LIVAS ALH depicts higher aerosol heights in spring than in summer, the OMI ALH shows the opposite. Several explanations are possible: 1) exclusion of OMI scenes with strong aerosol pollution episodes because of a too strict threshold applied on the OMI effective cloud fraction (see Sect. 6.1), 2) a more rigorous temperature correction should be applied on measured $N_{O_2-O_2}^s$ (assuming daily instead of seasonal temperature profiles), 3) inaccuracies of MODIS τ , 4) remaining small cloud residuals in OMI observations in spite of the strict applied filtering etc... All these elements should be further investigated.

Assuming that LIVAS ALH are here the reference, these results seem to present higher accuracy than the exercise of Park et al. (2016) showing a bias of 1 km of between retrieved OMI and the CALIPSO AEH values over ocean, during the Asian dust event on 31 March 2007. The reasons can be multiple: use of NNs instead of linear interpolation within a LUT, aerosol retrieved over land instead of ocean surfaces, consideration of variable surface albedos as inputs instead of a single value, application of a temperature correction on $N_{\text{O}_2-\text{O}_2}^{\text{s}}$, use of longer data records etc...

7 Conclusions

In this study, different Multilayer Perceptron Neural Network (NN) algorithms were developed and evaluated in order to retrieve aerosol layer height (ALH) over land from the OMI 477 nm O_2-O_2 spectral band. The aerosol height was here retrieved as aerosol layer pressure (ALP) and defined as the mid-pressure of an homogeneous scattering layer with a constant geometric thickness. The focus was on North-East Asia and cloud-free scenes dominated by scattering aerosol fine particles with Angstrom coefficient $\alpha = 1.5$, single scattering albedo ω_0 in the range of 0.9-0.95 and asymmetry parameter $g = 0.7$. The algorithms were trained with a large ensemble of synthetic data set and several precautions were taken into account to avoid over-training or local minima problems. The key concept of OMI ALP retrievals is the link between the measured O_2-O_2 slant column density (SCD) $N_{\text{O}_2-\text{O}_2}^{\text{s}}$ and the aerosol altitude as a consequence of shielding effect applied by the particles on the O_2-O_2 dimer complexes that are at lower altitudes. ALP was retrieved on 3 years 2005-2007 of OMI cloud-free observations collocated with MODIS-Aqua aerosol product in North-East Asia. The main objective of this work is first to evaluate the feasibility of a direct retrieval of this key aerosol parameter from a statistical point of view: i.e. over a long-time period and large industrialized continental area, and therefore a high number of observations. All the evaluated performances are summarized in Table 2

Analysis show that a good ALP retrieval requires an accurate prior knowledge of aerosol optical thickness τ as input information. Indeed, both τ and ALP parameters simultaneously contribute to the shielding of O_2-O_2 dimers. The analyses of $N_{\text{O}_2-\text{O}_2}^{\text{s}}$ alone leads to an ambiguity since aerosol extinction and aerosol altitude cannot be distinguished.

Because low amount of aerosols have very little impacts on $N_{\text{O}_2-\text{O}_2}^{\text{s}}$ changes, large biases are expected over scenes including aerosol particles with $\tau(550\text{nm}) \leq 0.5$. This $\tau(550\text{nm})$ value should be considered as a threshold for a good ALP retrieval quality. Moreover, the algorithms are expected to present a very low sensitivity to particles located at an altitude higher than 4 km. This is because of the nature of the O_2-O_2 complex of which the absorption scales with the pressure-squared instead of being linear with pressure.

Different NN configurations were tested. Sensitivity analysis on synthetic cases show that ALP accuracy with the best NN configuration (i.e. $NN_{\tau, N_{\text{O}_2-\text{O}_2}^{\text{s}}}$ algorithm with true $\tau(550\text{nm})$ value as input) lies in the range of 50-200 hPa (i.e. about 500 m and 1 km) over aerosol scenes with $\tau(550\text{nm})$ in the range of 0.5-1.0. The accuracy is improved to 0-50 hPa over scenes with $\tau(550\text{nm}) \geq 1.0$. Using the best available τ information is theoretically expected to limit the impact of uncertainties due to 1) aerosol model: bias in the range of 0-100 hPa if $\tau(550\text{nm}) \leq 1.0$, for a difference of 0.05 in ω_0 or for a difference of 0.1 in g , 2) surface albedo uncertainty in the range of 0.025-0.05 which leads to absolute ALP biases in the range of 50-100

hPa for τ between 0.5 and 1.0, and 0-50 hPa for $\tau(550\text{nm}) \geq 1.0$. Real ALH retrievals were performed over 3-year of OMI $\text{O}_2\text{-O}_2$ visible observations over cloud-free scenes with MODIS $\tau(550\text{nm}) \geq 1.0$ and using $NN_{\tau, N_{\text{O}_2\text{-O}_2}^s}$ combined with MODIS-Aqua $\tau(550\text{ nm})$. Comparison of seasonal and spatial averages with the LIVAS climatology database shows maximum (minimum) differences in the range of 260-800 (180-310) m, depending on the season and assuming $\omega_0 = 0.95$ ($\omega_0 = 0.9$).

5 Aerosol model assumptions (in particular ω_0) are the most critical as, in that configuration, they impact OMI seasonal-spatial averaged ALH in the range of 560-660 m. Changes due to the prior surface albedo database (OMLER or MODIS Black Sky) have a second order impact, up to 200 m.

In addition, algorithms should take into account that the $\text{O}_2\text{-O}_2$ SCD precision, resulting from the DOAS spectral fitting, affects the ALP retrieval. $\text{O}_2\text{-O}_2$ SCD precision lying in the range of $0.05\text{-}0.25 \cdot 10^{-43} \text{ mol}^2\text{cm}^{-5}$ leads to ALP precision
 10 between 19 ± 29 and 57 ± 31 hPa. Due to the nature of the $\text{O}_2\text{-O}_2$ collision complex, a temperature correction must be applied to the SCD prior to retrievals. Other parameters should be further investigated such as polarization effects and assumptions about the vertical distribution of particles.

An accuracy better than 0.2 must be required on prior $\tau(550\text{nm})$ information. Indeed, a $\tau(550\text{nm})$ bias of 0.25 is expected to bias the retrieved ALP up to 50 hPa for $\tau(550\text{nm})$ in the range of 0.6-1.0. For $\tau(550\text{nm}) \geq 1.0$, related ALP impacts almost
 15 become almost null. If no prior accurate τ information, such as from the MODIS aerosol Dark Target algorithm, is available, then this input parameter can be replaced by the OMI continuum reflectance $Rc(475\text{nm})$ (cf. the $NN_{Rc, N_{\text{O}_2\text{-O}_2}^s}$ algorithm). Indeed, this parameter is primarily affected by the aerosol amount and therefore contains information on $\tau(550\text{nm})$. It may then help to analyse $N_{\text{O}_2\text{-O}_2}^s$ for retrieving ALP provided that we can retrieve τ with a good quality.

Similarly to ALP retrieval, a NN algorithm was also developed to retrieve $\tau(550\text{nm})$ information from the OMI 477
 20 nm $\text{O}_2\text{-O}_2$ spectral band. However, its capability is strongly affected by uncertainties on the assumed aerosol model. An overestimation of aerosol single scattering albedo, from $\omega_0 = 0.9$ to 0.95, induces a negative bias of 0.8 for $\tau(550\text{nm}) = 2$. The impact is much lower for smaller τ (lower than 0.1 for $\tau(550\text{nm}) \leq 0.5$). Similar conclusions were found regarding uncertainty of the asymmetry parameter and thus the phase function characterization. Another major challenge when retrieving aerosol properties from passive satellite sensors is to separate the atmospheric and surface contributions in the total observed
 25 reflectance. Similarly to aerosol ω_0 , an overestimation of surface reflection leads to an underestimation of retrieved $\tau(550\text{nm})$. Surface albedo uncertainty below 0.025 should limit OMI retrieved $\tau(550\text{nm})$ bias smaller than 0.5 for $\tau(550\text{nm})$ in the range of 0.0-0.5, 0.25 for $\tau(550\text{nm}) = 2.0$. Comparisons of OMI retrievals with collocated MODIS $\tau(550\text{nm})$ show agreements between -0.02 ± 0.45 and -0.18 ± 0.24 depending on the seasons. Further improvements should be made before being able to use these OMI $\tau(550\text{nm})$ products as prior information to ALP retrievals.

30 Using the $NN_{Rc, N_{\text{O}_2\text{-O}_2}^s}$ algorithm for ALP retrieval is, in practice, similar to $NN_{\tau, N_{\text{O}_2\text{-O}_2}^s}$ combined with retrieved OMI $\tau(550\text{nm})$. Since, the retrieved OMI τ accuracy is lower than MODIS τ accuracy from the Dark target Land algorithm, $NN_{Rc, N_{\text{O}_2\text{-O}_2}^s}$ shows reduced performances and higher sensitivity to aerosol model and surface albedo uncertainties. Associated 3-year OMI ALH retrievals over North-East Asia are impacted by ω_0 uncertainties (0.9-0.95) in the range of 540-1200 m, and by surface albedo (OMLER vs. MODIS Black sky albedo) up to 730 m.

The NN approach presents, at this stage, quite promising results for a future operational processing of the OMI O₂–O₂ spectral band and the next UV-Vis satellite missions such as the TROPOspheric Monitoring Instrument (TROPOMI) (Veefkind et al., 2012). In spite of the high computing time due to the learning database creation and the training of these algorithms, very fast operational processing is allowed. Such processing is much faster than approaches relying on the Optimal Estimation Method and employs more optimized interpolation techniques than a classical linear interpolation within a LUT. For future processing of the OMI data, the OMLER climatology database should be optimized by filtering out small aerosol residuals.

Our study indicates that it is worthwhile to design and evaluate aerosol height retrieval algorithm exploiting the satellites 477 nm O₂–O₂ absorption band. Our long-term motivation is to evaluate the feasibility of replacing the effective clouds by more explicit aerosol parameters in the computation of trace gas AMF. This is relevant not only for OMI but for most of the UV-Vis satellite missions devoted to air quality monitoring. For that purpose, further analyses must be performed by focusing on significant geophysical variability cases: e.g. pixel-by-pixel variability over smaller regions. Furthermore, single OMI ALH retrievals should be compared with reference aerosol vertical profile measurements (ground-based and/or satellites) over some remarkable case studies.

Acknowledgements. This work was funded by the Netherlands Space Office (NSO) under the OMI contract. The authors thank Piet Stammes, Folkert Boersma and Maarten Sneep from KNMI for the discussions about aerosol simulations and measurements, and sharing their experience with respect to the DISAMAR software.

We thank all the developers of the PyBrain software. PyBrain is a joint project of PostDocs, PhD and master level students. The core programmers are (or were) students of Prof. Jurgen Schmidhuber at the Dalle Molle Institute for Artificial Intelligence in Switzerland and the Technische Universitat Munchen in Germany.

The LIVAS products have been collected from the LIVAS database (<http://lidar.space.noa.gr:8080/livas>), and were produced by the LIVAS team under the European Space Agency (ESA) study contract No. 4000104106/11/NL/FF/fk. We thank all the developers who have provided us with all the data set and for sharing their discussions and recommendations.

The developers of LIVAS would like to acknowledge support through the project MarcoPolo under grant agreement n° 606953 from the European Union Seventh Framework Program (FP7/2007-2013) and the research program ACTRIS-2 under grant agreement no. 654109 from the European Union's Horizon 2020 research and innovation program.

Finally, we thank the reviewers for their valuable and thorough work. This helps to consolidate the key messages of our study.

References

- Acarreta, J. R., de Haan, J. F., and Stammes, P.: Cloud pressure retrieval using the O₂–O₂ absorption band at 477 nm, *Journal of Geophysical Research: Atmospheres*, 109, n/a–n/a, doi:10.1029/2003JD003915, <http://dx.doi.org/10.1029/2003JD003915>, d05204, 2004.
- Ahn, C., Torres, O., and Jethva, H.: Assessment of OMI near-UV aerosol optical depth over land, *Journal of Geophysical Research: Atmospheres*, 119, 2457–2473, doi:10.1002/2013JD020188, <http://dx.doi.org/10.1002/2013JD020188>, 2013JD020188, 2014.
- Amiridis, V., Marinou, E., Tsekeri, A., Wandinger, U., Schwarz, A., Giannakaki, E., Mamouri, R., Kokkalis, P., Biniotoglou, I., Solomos, S., Herekakis, T., Kazadzis, S., Gerasopoulos, E., Proestakis, E., Kottas, M., Balis, D., Papayannis, A., Kontoes, C., Kourtidis, K., Papagiannopoulos, N., Mona, L., Pappalardo, G., Le Rille, O., and Ansmann, A.: LIVAS: a 3-D multi-wavelength aerosol/cloud database based on CALIPSO and EARLINET, *Atmospheric Chemistry and Physics*, 15, 7127–7153, doi:10.5194/acp-15-7127-2015, <http://www.atmos-chem-phys.net/15/7127/2015/>, 2015.
- Atkinson, P. M. and Tatnall, A. R. L.: Introduction Neural networks in remote sensing, *International Journal of Remote Sensing*, 18, 699–709, doi:10.1080/014311697218700, <http://dx.doi.org/10.1080/014311697218700>, 1997.
- Barkley, M. P., Kurosu, T. P., Chance, K., De Smedt, I., Van Roozendaal, M., Arneth, A., Hagberg, D., and Guenther, A.: Assessing sources of uncertainty in formaldehyde air mass factors over tropical South America: Implications for top-down isoprene emission estimates, *Journal of Geophysical Research: Atmospheres*, 117, n/a–n/a, doi:10.1029/2011JD016827, <http://dx.doi.org/10.1029/2011JD016827>, d13304, 2012.
- Barkley, M. P., De Smedt, I., VanRoozendaal, M., Kurosu, T. P., Chance, K., Arneth, A., Hagberg, D., Guenther, A., Paulot, F., Marais, E., and Mao, J.: Top-down isoprene emissions over tropical South America inferred from SCIAMACHY and OMI formaldehyde columns, *Journal of Geophysical Research: Atmospheres*, 118, 6849–6868, doi:10.1002/jgrd.50552, <http://dx.doi.org/10.1002/jgrd.50552>, 2013.
- Boersma, K. F., Eskes, H. J., Veefkind, J. P., Brinksma, E. J., van der A, R. J., Sneep, M., van den Oord, G. H. J., Levelt, P. F., Stammes, P., Gleason, J. F., and Bucsele, E. J.: Near-real time retrieval of tropospheric NO₂ from OMI, *Atmospheric Chemistry and Physics*, 7, 2103–2118, doi:10.5194/acp-7-2103-2007, <http://www.atmos-chem-phys.net/7/2103/2007/>, 2007.
- Boersma, K. F., Eskes, H. J., Dirksen, R. J., van der A, R. J., Veefkind, J. P., Stammes, P., Huijnen, V., Kleipool, Q. L., Sneep, M., Claas, J., Leitao, J., Richter, A., Zhou, Y., and Brunner, D.: An improved tropospheric NO₂ column retrieval algorithm for the Ozone Monitoring Instrument, *Atmospheric Measurement Techniques*, 4, 1905–1928, doi:10.5194/amt-4-1905-2011, <http://www.atmos-meas-tech.net/4/1905/2011/>, 2011.
- Castellanos, P., Boersma, K. F., Torres, O., and de Haan, J. F.: OMI tropospheric NO₂ air mass factors over South America: effects of biomass burning aerosols, *Atmospheric Measurement Techniques*, 8, 3831–3849, doi:10.5194/amt-8-3831-2015, <http://www.atmos-meas-tech.net/8/3831/2015/>, 2015.
- Chameides, W. L., Yu, H., Liu, S. C., Bergin, M., Zhou, X., Mearns, L., Wang, G., Kiang, C. S., Saylor, R. D., Luo, C., Huang, Y., Steiner, A., and Giorgi, F.: Case study of the effects of atmospheric aerosols and regional haze on agriculture: An opportunity to enhance crop yields in China through emission controls?, *Proceedings of the National Academy of Sciences*, 96, 13 626–13 633, doi:10.1073/pnas.96.24.13626, <http://www.pnas.org/content/96/24/13626.abstract>, 1999.
- Chimot, J., Vlemmix, T., Veefkind, J. P., de Haan, J. F., and Levelt, P. F.: Impact of aerosols on the OMI tropospheric NO₂ retrievals over industrialized regions: how accurate is the aerosol correction of cloud-free scenes via a simple cloud model?, *Atmospheric Measurement Techniques*, 9, 359–382, doi:10.5194/amt-9-359-2016, <http://www.atmos-meas-tech.net/9/359/2016/>, 2016.

- Crevoisier, C., Chédin, A., Matsueda, H., Machida, T., Armante, R., and Scott, N. A.: First year of upper tropospheric integrated content of CO₂ from IASI hyperspectral infrared observations, *Atmospheric Chemistry and Physics*, 9, 4797–4810, doi:10.5194/acp-9-4797-2009, <http://www.atmos-chem-phys.net/9/4797/2009/>, 2009a.
- Crevoisier, C., Nobileau, D., Fiore, A. M., Armante, R., Chédin, A., and Scott, N. A.: Tropospheric methane in the tropics – first year from IASI hyperspectral infrared observations, *Atmospheric Chemistry and Physics*, 9, 6337–6350, doi:10.5194/acp-9-6337-2009, <http://www.atmos-chem-phys.net/9/6337/2009/>, 2009b.
- de Graaf, M., Stammes, P., Torres, O., and Koelemeijer, R. B. A.: Absorbing Aerosol Index: Sensitivity analysis, application to GOME and comparison with TOMS, *Journal of Geophysical Research: Atmospheres*, 110, n/a–n/a, doi:10.1029/2004JD005178, <http://dx.doi.org/10.1029/2004JD005178>, d01201, 2005.
- de Haan, J. F.: DISAMAR Algorithm Description and Background Information, Royal Netherlands Meteorological Institute, De Bilt, the Netherlands, 2011.
- de Haan, J. F., Bosma, P. B., and Hovenier, J. W.: The adding method for multiple scattering calculations of polarized light, , 183, 371–391, <http://adsabs.harvard.edu/abs/1987A%26A...183..371D>, provided by the SAO/NASA Astrophysics Data System, 1987.
- de Leeuw, G., Holzer-Popp, T., Bevan, S., Davies, W. H., Descloitres, J., Grainger, R. G., Griesfeller, J., Heckel, A., Kinne, S., Klüser, L., Kolmonen, P., Litvinov, P., Martynenko, D., North, P., Ovigneur, B., Pascal, N., Poulsen, C., Ramon, D., Schulz, M., Siddans, R., Sogacheva, L., Tanré, D., Thomas, G. E., Virtanen, T. H., von Hoyningen Huene, W., Vountas, M., and Pinnock, S.: Evaluation of seven European aerosol optical depth retrieval algorithms for climate analysis, *Remote Sensing of Environment*, 162, 295 – 315, doi:<http://dx.doi.org/10.1016/j.rse.2013.04.023>, <http://www.sciencedirect.com/science/article/pii/S0034425713003507>, 2013.
- de Smedt, I., Müller, J.-F., Stavrakou, T., van der A, R., Eskes, H., and Van Roozendael, M.: Twelve years of global observations of formaldehyde in the troposphere using GOME and SCIAMACHY sensors, *Atmospheric Chemistry and Physics*, 8, 4947–4963, doi:10.5194/acp-8-4947-2008, <http://www.atmos-chem-phys.net/8/4947/2008/>, 2008.
- Di Noia, A., Hasekamp, O. P., van Harten, G., Rietjens, J. H. H., Smit, J. M., Snik, F., Henzing, J. S., de Boer, J., Keller, C. U., and Volten, H.: Use of neural networks in ground-based aerosol retrievals from multi-angle spectropolarimetric observations, *Atmospheric Measurement Techniques*, 8, 281–299, doi:10.5194/amt-8-281-2015, <http://www.atmos-meas-tech.net/8/281/2015/>, 2015.
- Dirksen, R. J., Folkert Boersma, K., de Laat, J., Stammes, P., van der Werf, G. R., Val Martin, M., and Kelder, H. M.: An aerosol boomerang: Rapid around-the-world transport of smoke from the December 2006 Australian forest fires observed from space, *Journal of Geophysical Research: Atmospheres*, 114, n/a–n/a, doi:10.1029/2009JD012360, <http://dx.doi.org/10.1029/2009JD012360>, d21201, 2009.
- Dubovik, O., Holben, B., Eck, T. F., Smirnov, A., Kaufman, Y. J., King, M. D., Tanré, D., and Slutsker, I.: Variability of Absorption and Optical Properties of Key Aerosol Types Observed in Worldwide Locations, *Journal of the Atmospheric Sciences*, 59, 590–608, doi:10.1175/1520-0469(2002)059<0590:VOAAOP>2.0.CO;2, [http://dx.doi.org/10.1175/1520-0469\(2002\)059<0590:VOAAOP>2.0.CO;2](http://dx.doi.org/10.1175/1520-0469(2002)059<0590:VOAAOP>2.0.CO;2), 2, 2002.
- Dufresne, J.-L., Gautier, C., Ricchiazzi, P., and Fouquart, Y.: Longwave Scattering Effects of Mineral Aerosols, *Journal of the Atmospheric Sciences*, 59, 1959–1966, doi:10.1175/1520-0469(2002)059<1959:LSEOMA>2.0.CO;2, [http://dx.doi.org/10.1175/1520-0469\(2002\)059<1959:LSEOMA>2.0.CO;2](http://dx.doi.org/10.1175/1520-0469(2002)059<1959:LSEOMA>2.0.CO;2), 2, 2002.
- Eck, T. F., Holben, B. N., Dubovik, O., Smirnov, A., Goloub, P., Chen, H. B., Chatenet, B., Gomes, L., Zhang, X.-Y., Tsay, S.-C., Ji, Q., Giles, D., and Slutsker, I.: Columnar aerosol optical properties at AERONET sites in central eastern Asia and aerosol transport to the tropical mid-Pacific, *Journal of Geophysical Research: Atmospheres*, 110, n/a–n/a, doi:10.1029/2004JD005274, <http://dx.doi.org/10.1029/2004JD005274>, d06202, 2005.

- Feingold, G., Cotton, W. R., Kreidenweis, S. M., Janel, and Davis, T.: The impact of giant cloud condensation nuclei on drizzle formation in stratocumulus: Implications for cloud radiative properties, *J. Atmos. Sci.*, pp. 4100–4117, 1999.
- Haykin, S.: *Neural Networks: A Comprehensive Foundation*, International edition, Prentice Hall, <https://books.google.com.tr/books?id=M5abQgAACAAJ>, 1999.
- 5 Hewson, W., Barkley, M. P., Gonzalez Abad, G., Bösch, H., Kurosu, T., Spurr, R., and Tilstra, L. G.: Development and characterisation of a state-of-the-art GOME-2 formaldehyde air-mass factor algorithm, *Atmospheric Measurement Techniques*, 8, 4055–4074, doi:10.5194/amt-8-4055-2015, <http://www.atmos-meas-tech.net/8/4055/2015/>, 2015.
- Hovenier, J. W. and Hage, J. I.: Relations involving the spherical albedo and other photometric quantities of planets with thick atmospheres, , 214, 391–401, <http://adsabs.harvard.edu/abs/1989A%26A...214..391H>, provided by the SAO/NASA Astrophysics Data System, 1989.
- 10 IPCC: Solomon, S., Qin, D., Manning, M., Chen, Z., M., M., Averyt, K. B., Tignor, M., and Miller, H. L.: *Climate Change 2007: The Physical Science Basis. Contribution of Working Group I to the Fourth Assessment Report of the Intergovernmental Panel on Climate Change*, Cambridge University Press, Cambridge, United Kingdom and New York, NY, USA, 2007.
- IPCC: The Core Writing Team Pachauri, R. K. and Meyer, L. A.: *Climate Change 2014: Synthesis Report. Contribution of Working Groups I, II and III to the Fifth Assessment Report of the Intergovernmental Panel on Climate Change*, IPCC, Geneva, Switzerland, <http://www.ipcc.ch/report/ar5/syr/>, 2014.
- 15 Jethva, H., Torres, O., and Ahn, C.: Global assessment of OMI aerosol single-scattering albedo using ground-based AERONET inversion, *Journal of Geophysical Research: Atmospheres*, 119, 9020–9040, doi:10.1002/2014JD021672, <http://dx.doi.org/10.1002/2014JD021672>, 2014JD021672, 2014.
- Kanaya, Y., Irie, H., Takashima, H., Iwabuchi, H., Akimoto, H., Sudo, K., Gu, M., Chong, J., Kim, Y. J., Lee, H., Li, A., Si, F., Xu, J., Xie, P.-H., Liu, W.-Q., Dzhola, A., Postlyakov, O., Ivanov, V., Grechko, E., Terpugova, S., and Panchenko, M.: Long-term MAX-DOAS network observations of NO₂ in Russia and Asia (MADRAS) during the period 2007 and 2012: instrumentation, elucidation of climatology, and comparisons with OMI satellite observations and global model simulations, *Atmospheric Chemistry and Physics*, 14, 7909–7927, doi:10.5194/acp-14-7909-2014, <http://www.atmos-chem-phys.net/14/7909/2014/>, 2014.
- 20 Kaufman, Y. J., Tanre, D., and Boucher, O.: A satellite view of aerosols in the climate system, *Nature*, 419, 215–223, doi:10.1038/nature01091, <http://dx.doi.org/10.1038/nature01091>, 2002.
- 25 Kleipool, Q. L., Dobber, M. R., de Haan, J. F., and Levelt, P. F.: Earth surface reflectance climatology from 3 years of OMI data, *Journal of Geophysical Research: Atmospheres*, 113, n/a–n/a, doi:10.1029/2008JD010290, <http://dx.doi.org/10.1029/2008JD010290>, d18308, 2008.
- Koelemeijer, R. B. A., de Haan, J. F., and Stammes, P.: A database of spectral surface reflectivity in the range 335–772 nm derived from 5.5 years of GOME observations, *Journal of Geophysical Research: Atmospheres*, 108, n/a–n/a, doi:10.1029/2002JD002429, <http://dx.doi.org/10.1029/2002JD002429>, 4070, 2003.
- 30 Krotkov, N. A., McClure, B., Dickerson, R. R., Carn, S. A., Li, C., Bhartia, P. K., Yang, K., Krueger, A. J., Li, Z., Levelt, P. F., Chen, H., Wang, P., and Lu, D.: Validation of SO₂ retrievals from the Ozone Monitoring Instrument over NE China, *Journal of Geophysical Research: Atmospheres*, 113, n/a–n/a, doi:10.1029/2007JD008818, <http://dx.doi.org/10.1029/2007JD008818>, d16S40, 2008.
- Kuhlmann, G., Lam, Y. F., Cheung, H. M., Hartl, A., Fung, J. C. H., Chan, P. W., and Wenig, M. O.: Development of a custom OMI NO₂ data product for evaluating biases in a regional chemistry transport model, *Atmospheric Chemistry and Physics*, 15, 5627–5644, doi:10.5194/acp-15-5627-2015, <http://www.atmos-chem-phys.net/15/5627/2015/>, 2015.
- 35

- Lee, C., Martin, R. V., van Donkelaar, A., O’Byrne, G., Krotkov, N., Richter, A., Huey, L. G., and Holloway, J. S.: Retrieval of vertical columns of sulfur dioxide from SCIAMACHY and OMI: Air mass factor algorithm development, validation, and error analysis, *Journal of Geophysical Research: Atmospheres*, 114, n/a–n/a, doi:10.1029/2009JD012123, <http://dx.doi.org/10.1029/2009JD012123>, d22303, 2009.
- Lee, J., Kim, J., Yang, P., and Hsu, N. C.: Improvement of aerosol optical depth retrieval from MODIS spectral reflectance over the global ocean using new aerosol models archived from AERONET inversion data and tri-axial ellipsoidal dust database, *Atmospheric Chemistry and Physics*, 12, 7087–7102, doi:10.5194/acp-12-7087-2012, <http://www.atmos-chem-phys.net/12/7087/2012/>, 2012.
- Lee, K. H., Li, Z., Wong, M. S., Xin, J., Wang, Y., Hao, W.-M., and Zhao, F.: Aerosol single scattering albedo estimated across China from a combination of ground and satellite measurements, *Journal of Geophysical Research (Atmospheres)*, 112, D22S15, doi:10.1029/2007JD009077, 2007.
- 10 Leitão, J., Richter, A., Vrekoussis, M., Kokhanovsky, A., Zhang, Q. J., Beekmann, M., and Burrows, J. P.: On the improvement of NO₂ satellite retrievals – aerosol impact on the air mass factors, *Atmospheric Measurement Techniques*, 3, 475–493, doi:10.5194/amt-3-475-2010, <http://www.atmos-meas-tech.net/3/475/2010/>, 2010.
- Levelt, P. F., Hilsenrath, E., Leppelmeier, G. W., van den Oord, G. H. J., Bhartia, P. K., Tamminen, J., de Haan, J. F., and Veeffkind, J. P.: Science Objectives of the Ozone Monitoring Instrument, *IEEE Transactions on Geoscience and Remote Sensing*, 44, 1199–1208, doi:10.1109/TGRS.2006.872336, 2006.
- 15 Levy, R. C., Remer, L. A., Mattoo, S., Vermote, E. F., and Kaufman, Y. J.: Second-generation operational algorithm: Retrieval of aerosol properties over land from inversion of Moderate Resolution Imaging Spectroradiometer spectral reflectance, *Journal of Geophysical Research: Atmospheres*, 112, n/a–n/a, doi:10.1029/2006JD007811, <http://dx.doi.org/10.1029/2006JD007811>, d13211, 2007.
- Levy, R. C., Mattoo, S., Munchak, L. A., Remer, L. A., Sayer, A. M., Patadia, F., and Hsu, N. C.: The Collection 6 MODIS aerosol products over land and ocean, *Atmospheric Measurement Techniques*, 6, 2989–3034, doi:10.5194/amt-6-2989-2013, <http://www.atmos-meas-tech.net/6/2989/2013/>, 2013.
- 20 Lin, J.-T., Martin, R. V., Boersma, K. F., Sneep, M., Stammes, P., Spurr, R., Wang, P., Van Roozendaal, M., Clémer, K., and Irie, H.: Retrieving tropospheric nitrogen dioxide from the Ozone Monitoring Instrument: effects of aerosols, surface reflectance anisotropy, and vertical profile of nitrogen dioxide, *Atmospheric Chemistry and Physics*, 14, 1441–1461, doi:10.5194/acp-14-1441-2014, <http://www.atmos-chem-phys.net/14/1441/2014/>, 2014.
- 25 Lin, J.-T., Liu, M.-Y., Xin, J.-Y., Boersma, K. F., Spurr, R., Martin, R., and Zhang, Q.: Influence of aerosols and surface reflectance on satellite NO₂ retrieval: seasonal and spatial characteristics and implications for NO_x emission constraints, *Atmospheric Chemistry and Physics*, 15, 11 217–11 241, doi:10.5194/acp-15-11217-2015, <http://www.atmos-chem-phys.net/15/11217/2015/>, 2015.
- Loyola, D.: Automatic cloud analysis from polar-orbiting satellites using neural network and data fusion techniques, in: *IGARSS 2004. 2004 IEEE International Geoscience and Remote Sensing Symposium*, vol. 4, pp. 2530–2533 vol.4, doi:10.1109/IGARSS.2004.1369811, 2004.
- 30 Loyola, D., Thomas, W., Livschitz, Y., Ruppert, T., Albert, P., and Hollmann, R.: Cloud Properties Derived From GOME/ERS-2 Backscatter Data for Trace Gas Retrieval, *IEEE Transactions on Geoscience and Remote Sensing*, 45, 2747–2758, doi:10.1109/TGRS.2007.901043, 2007.
- Loyola, D., Thomas, W., Spurr, R., and Mayer, B.: Global patterns in daytime cloud properties derived from GOME backscatter UV-VIS measurements, *International Journal of Remote Sensing*, 31, 4295–4318, doi:10.1080/01431160903246741, <http://dx.doi.org/10.1080/01431160903246741>, 2010.
- 35

- Luger, G. and Stubblefield, W.: Artificial intelligence : Structures and strategies for complex problem solving, Benjamin/Cummings, http://www.worldcat.org/title/artificial-intelligence-structures-and-strategies-for-complex-problem-solving/oclc/26305570&referer=brief_results, 1998.
- Lyapustin, A., Wang, Y., Xiong, X., Meister, G., Platnick, S., Levy, R., Franz, B., Korkin, S., Hilker, T., Tucker, J., Hall, F., Sellers, P., Wu, A.,
5 and Angal, A.: Scientific impact of MODIS C5 calibration degradation and C6+ improvements, *Atmospheric Measurement Techniques*, 7, 4353–4365, doi:10.5194/amt-7-4353-2014, <http://www.atmos-meas-tech.net/7/4353/2014/>, 2014.
- Ma, J. Z., Beirle, S., Jin, J. L., Shaiganfar, R., Yan, P., and Wagner, T.: Tropospheric NO₂ vertical column densities over Beijing: results of the first three years of ground-based MAX-DOAS measurements (2008 and 2011) and satellite validation, *Atmospheric Chemistry and Physics*, 13, 1547–1567, doi:10.5194/acp-13-1547-2013, <http://www.atmos-chem-phys.net/13/1547/2013/>, 2013.
- 10 Omar, A. H., Winker, D. M., Vaughan, M. A., Hu, Y., Trepte, C. R., Ferrare, R. A., Lee, K.-P., Hostetler, C. A., Kittaka, C., Rogers, R. R., Kuehn, R. E., and Liu, Z.: The CALIPSO Automated Aerosol Classification and Lidar Ratio Selection Algorithm, *Journal of Atmospheric and Oceanic Technology*, 26, 1994–2014, doi:10.1175/2009JTECHA1231.1, <http://dx.doi.org/10.1175/2009JTECHA1231.1>, 2009.
- Park, S. S., Kim, J., Lee, H., Torres, O., Lee, K.-M., and Lee, S. D.: Utilization of O₄ slant column density to derive aerosol layer height from a space-borne UV–visible hyperspectral sensor: sensitivity and case study, *Atmospheric Chemistry and Physics*, 16, 1987–2006,
15 doi:10.5194/acp-16-1987-2016, <http://www.atmos-chem-phys.net/16/1987/2016/>, 2016.
- Platt, U. and Stutz, J.: Differential Optical Absorption Spectroscopy (DOAS), Principles and Applications, doi:10.1007/978-3-540-75776-4, 2008.
- Prospero, J. M.: Long-term measurements of the transport of African mineral dust to the southeastern United States: Implications for regional air quality, , 104, 15, doi:10.1029/1999JD900072, 1999.
- 20 Ramanathan, V., Crutzen, P. J., Kiehl, J. T., and Rosenfeld, D.: Aerosols, Climate, and the Hydrological Cycle, *Science*, 294, 2119–2124, doi:10.1126/science.1064034, <http://science.sciencemag.org/content/294/5549/2119>, 2001.
- Rosenfeld, D.: Suppression of Rain and Snow by Urban and Industrial Air Pollution, *Science*, 287, 1793–1796, doi:10.1126/science.287.5459.1793, <http://science.sciencemag.org/content/287/5459/1793>, 2000.
- Rosenfeld, D., Lahav, R., Khain, A., and Pinsky, M.: The Role of Sea Spray in Cleansing Air Pollution over Ocean via Cloud Processes,
25 *Science*, 297, 1667–1670, doi:10.1126/science.1073869, <http://science.sciencemag.org/content/297/5587/1667>, 2002.
- Rumelhart, D. E., Hinton, G. E., and Williams, R. J.: Learning representations by back-propagating errors, *Nature*, 323, 533–536, doi:10.1038/323533a0, <http://dx.doi.org/10.1038/323533a0>, 1986.
- Sanders, A. F. J., de Haan, J. F., Sneep, M., Apituley, A., Stammes, P., Vieitez, M. O., Tilstra, L. G., Tuinder, O. N. E., Koning, C. E., and Veefkind, J. P.: Evaluation of the operational Aerosol Layer Height retrieval algorithm for Sentinel-5 Precursor: application to O₂ A
30 band observations from GOME-2A, *Atmospheric Measurement Techniques*, 8, 4947–4977, doi:10.5194/amt-8-4947-2015, <http://www.atmos-meas-tech.net/8/4947/2015/>, 2015.
- Sayer, A. M., Hsu, N. C., Bettenhausen, C., and Jeong, M.-J.: Validation and uncertainty estimates for MODIS Collection 6 “Deep Blue” aerosol data, *Journal of Geophysical Research: Atmospheres*, 118, 7864–7872, doi:10.1002/jgrd.50600, <http://dx.doi.org/10.1002/jgrd.50600>, 2013.
- 35 Schaaf, C. B., Gao, F., Strahler, A. H., Lucht, W., Li, X., Tsang, T., Strugnell, N. C., Zhang, X., Jin, Y., Muller, J.-P., Lewis, P., Barnesley, M., Hobson, P., Disney, M., Roberts, G., Dunderdale, M., Doll, C., d’Entremont, R. P., Hu, B., Liang, S., Privette, J. L., and Roy, D.: First operational BRDF, albedo nadir reflectance products from {MODIS}, *Remote Sensing of Environment*, 83, 135 – 148,

- doi:[http://dx.doi.org/10.1016/S0034-4257\(02\)00091-3](http://dx.doi.org/10.1016/S0034-4257(02)00091-3), <http://www.sciencedirect.com/science/article/pii/S0034425702000913>, the Moderate Resolution Imaging Spectroradiometer (MODIS): a new generation of Land Surface Monitoring, 2002.
- Schaul, T., Bayer, J., Wierstra, D., Sun, Y., Felder, M., Sehnke, F., Rückstieß, T., and Schmidhuber, J.: PyBrain, *Journal of Machine Learning Research*, 11, 746–746, doi:10.1.1.193.3547, <http://citeseerx.ist.psu.edu/viewdoc/summary?doi=10.1.1.193.3547>, 2010.
- 5 Shaiganfar, R., Beirle, S., Sharma, M., Chauhan, A., Singh, R. P., and Wagner, T.: Estimation of NO_x emissions from Delhi using Car MAX-DOAS observations and comparison with OMI satellite data, *Atmospheric Chemistry and Physics*, 11, 10871–10887, doi:10.5194/acp-11-10871-2011, <http://www.atmos-chem-phys.net/11/10871/2011/>, 2011.
- Sneep, M., de Haan, J. F., Stammes, P., Wang, P., Vanbauce, C., Joiner, J., Vasilkov, A. P., and Levelt, P. F.: Three-way comparison between OMI and PARASOL cloud pressure products, *Journal of Geophysical Research: Atmospheres*, 113, n/a–n/a, doi:10.1029/2007JD008694, 10 <http://dx.doi.org/10.1029/2007JD008694>, d15S23, 2008.
- Sontag, E. D.: Feedback stabilization using two-hidden-layer nets, *IEEE Transactions on Neural Networks*, 3, 981–990, doi:10.1109/72.165599, 1992.
- Spada, F., Krol, M. C., and Stammes, P.: McSCIA: application of the Equivalence Theorem in a Monte Carlo radiative transfer model for spherical shell atmospheres, *Atmospheric Chemistry and Physics*, 6, 4823–4842, doi:10.5194/acp-6-4823-2006, <http://www.atmos-chem-phys.net/6/4823/2006/>, 2006.
- 15 Stammes, P.: Spectral radiance modelling in the UV-visible range, in *Proceedings IRS-2000: Current Problems in Atmospheric Radiation, Studies in geophysical optics and remote sensing*, A deepak publishing, 101 Research drive, PO BOX 7390, Hampton, VA 23666 USA, http://apps.webofknowledge.com/InboundService.do?product=WOS&SID=P1RNz4xEQjDzvcN8Fu&UT=WOS%3A000176920100100&SrcApp=Wiley_Online_Library&DestFail=http%3A%2F%2Fwww.webofknowledge.com&action=retrieve&Init=Yes&SrcAuth=LinksAMR&Func=Frame&customersID=LinksAMR&IsProductCode=Yes&mode=FullRecord, 2001.
- 20 Torres, O., Bhartia, P. K., Herman, J. R., Ahmad, Z., and Gleason, J.: Derivation of aerosol properties from satellite measurements of backscattered ultraviolet radiation: Theoretical basis, *Journal of Geophysical Research: Atmospheres*, 103, 17099–17110, doi:10.1029/98JD00900, <http://dx.doi.org/10.1029/98JD00900>, 1998.
- Torres, O., Bhartia, P. K., Herman, J. R., Sinyuk, A., Ginoux, P., and Holben, B.: A Long-Term Record of Aerosol Optical Depth from TOMS Observations and Comparison to AERONET Measurements., *Journal of Atmospheric Sciences*, 59, 398–413, doi:10.1175/1520-0469(2002)059<0398:ALTROA>2.0.CO;2, 2002.
- 25 Torres, O., Tanskanen, A., Veihelmann, B., Ahn, C., Braak, R., Bhartia, P. K., Veefkind, P., and Levelt, P.: Aerosols and surface UV products from Ozone Monitoring Instrument observations: An overview, *Journal of Geophysical Research: Atmospheres*, 112, n/a–n/a, doi:10.1029/2007JD008809, <http://dx.doi.org/10.1029/2007JD008809>, d24S47, 2007.
- 30 Torres, O., Ahn, C., and Chen, Z.: Improvements to the OMI near-UV aerosol algorithm using A-train CALIOP and AIRS observations, *Atmospheric Measurement Techniques*, 6, 3257–3270, doi:10.5194/amt-6-3257-2013, <http://www.atmos-meas-tech.net/6/3257/2013/>, 2013.
- Twomey, S. A., Piegras, M., and Wolfe, T. L.: An assessment of the impact of pollution on global cloud albedo, *Tellus B*, 36B, 356–366, doi:10.1111/j.1600-0889.1984.tb00254.x, <http://dx.doi.org/10.1111/j.1600-0889.1984.tb00254.x>, 1984.
- Veefkind, J. P., Boersma, K. F., Wang, J., Kurosu, T. P., Krotkov, N., Chance, K., and Levelt, P. F.: Global satellite analysis of the relation between aerosols and short-lived trace gases, *Atmospheric Chemistry and Physics*, 11, 1255–1267, doi:10.5194/acp-11-1255-2011, <http://www.atmos-chem-phys.net/11/1255/2011/>, 2011.
- 35 Veefkind, J. P., Aben, I., McMullan, K., Förster, H., de Vries, J., Otter, G., Claas, J., Eskes, H. J., de Haan, J. F., Kleipool, Q., van Weele, M., Hasekamp, O., Hoogeveen, R., Landgraf, J., Snel, R., Tol, P., Ingmann, P., Voors, R., Kruizinga, B., Vink, R., Visser, H., and Levelt,

Table 1. Ensemble of parameters and values associated with the synthetic learning data set (see Sect. 3.2). Aerosols are simulated with a Henyey-Greenstein scattering phase function (Hovenier and Hage, 1989)

Parameter	List of values
Solar Zenith Angle (θ_0) [$^\circ$]	9.267, 21.167, 32.892, 44.217, 54.940, 64.814
Viewing Zenith Angle (θ) [$^\circ$]	0.0, 9.267, 21.167, 32.892, 44.217
Relative azimuth angle ($\phi - \phi_0$) [$^\circ$]	0., 30., 60., 90., 120., 150., 180.
Surface pressure (P_s) [hPa]	1013., 963.
Surface albedo (A)	0.025, 0.05, 0.075, 0.1
$\tau(550\text{nm})$	0.0, 0.05, 0.1, 0.2, 0.4, 0.5, 0.6, 0.9, 1.25, 2.0, 3.0
Aerosol layer pressure (ALP) [hPa]	975., 925., 850., 750., 700., 650., 550., 350., 150.
Aerosol Single Scattering Albedo (ω_0)	0.9, 0.95
Ångström coefficient (α)	1.5
asymmetry parameter (g)	0.7

P. F.: TROPOMI on the ESA Sentinel-5 Precursor: A GMES mission for global observations of the atmospheric composition for climate, air quality and ozone layer applications, Remote sensing of environment., 120, 70–83, doi:10.1016/j.rse.2011.09.027, <http://dx.doi.org/10.1016/j.rse.2011.09.027>, 2012.

5 Veefkind, J. P., de Haan, J. F., Sneep, M., and Levelt, P. F.: Improvements of the OMI O₂–O₂ Operational Cloud Algorithm and Comparisons with Ground-Based Radar-Lidar Observations, Atmospheric Measurement Techniques Discussions, 2016, 1–28, doi:10.5194/amt-2016-48, <http://www.atmos-meas-tech-discuss.net/amt-2016-48/>, 2016.

Veihelmann, B., Levelt, P. F., Stammes, P., and Veefkind, J. P.: Simulation study of the aerosol information content in OMI spectral reflectance measurements, Atmospheric Chemistry and Physics, 7, 3115–3127, doi:10.5194/acp-7-3115-2007, <http://www.atmos-chem-phys.net/7/3115/2007/>, 2007.

10 Wagner, T., Burrows, J. P., Deutschmann, T., Dix, B., von Friedeburg, C., Frieß, U., Hendrick, F., Heue, K.-P., Irie, H., Iwabuchi, H., Kanaya, Y., Keller, J., McLinden, C. A., Oetjen, H., Palazzi, E., Petritoli, A., Platt, U., Postlyakov, O., Pukite, J., Richter, A., van Roozendaal, M., Rozanov, A., Rozanov, V., Sinreich, R., Sanghavi, S., and Wittrock, F.: Comparison of box-air-mass-factors and radiances for Multiple-Axis Differential Optical Absorption Spectroscopy (MAX-DOAS) geometries calculated from different UV/visible radiative transfer models, Atmospheric Chemistry and Physics, 7, 1809–1833, doi:10.5194/acp-7-1809-2007, <http://www.atmos-chem-phys.net/7/1809/2007/>, 2007.

15 Xiao, Q., Zhang, H., Choi, M., Li, S., Kondragunta, S., Kim, J., Holben, B., Levy, R. C., and Liu, Y.: Evaluation of VIIRS, GOCI, and MODIS Collection 6 AOD retrievals against ground sunphotometer observations over East Asia, Atmospheric Chemistry and Physics, 16, 1255–1269, doi:10.5194/acp-16-1255-2016, <http://www.atmos-chem-phys.net/16/1255/2016/>, 2016.

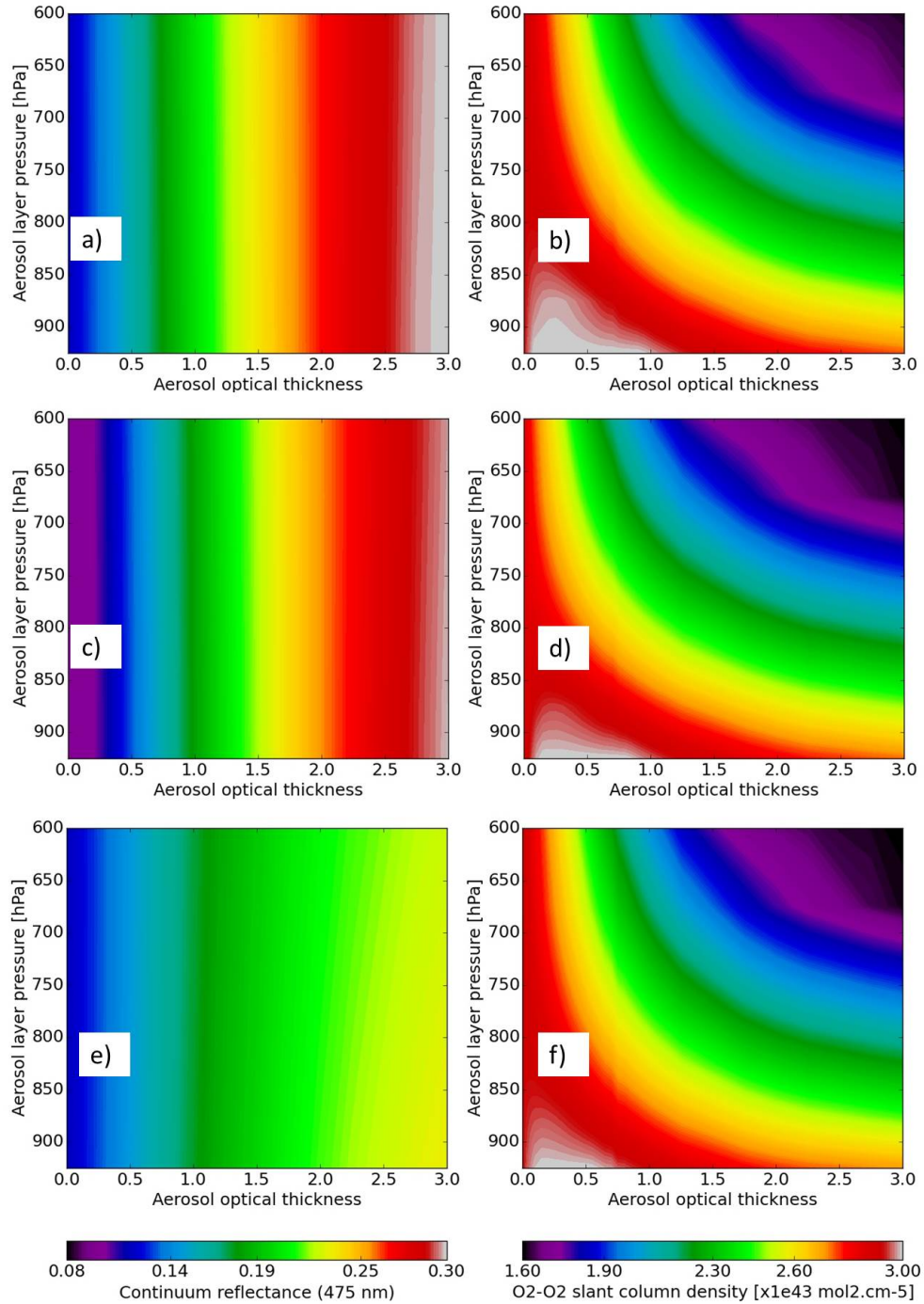


Figure 1. Continuum reflectance $R_c(475nm)$ and O_2-O_2 slant column density $N_{O_2-O_2}^s$ as a function of $\tau(550nm)$ and aerosol layer pressure for the following conditions: climatology mid-latitude summer temperature, NO_2 , O_3 and H_2O profiles, $\theta_0 = 32^\circ$, $\theta = 32^\circ$, surface pressure = 1010 hPa and fine aerosol particles ($\alpha = 1.5$, $g = 0.7$): (a) and (b) surface albedo = 0.07 and aerosol $\omega_0 = 0.95$, (c) and (d) surface albedo = 0.03 and aerosol $\omega_0 = 0.95$, (e) and (f) surface albedo = 0.07 and aerosol $\omega_0 = 0.9$.

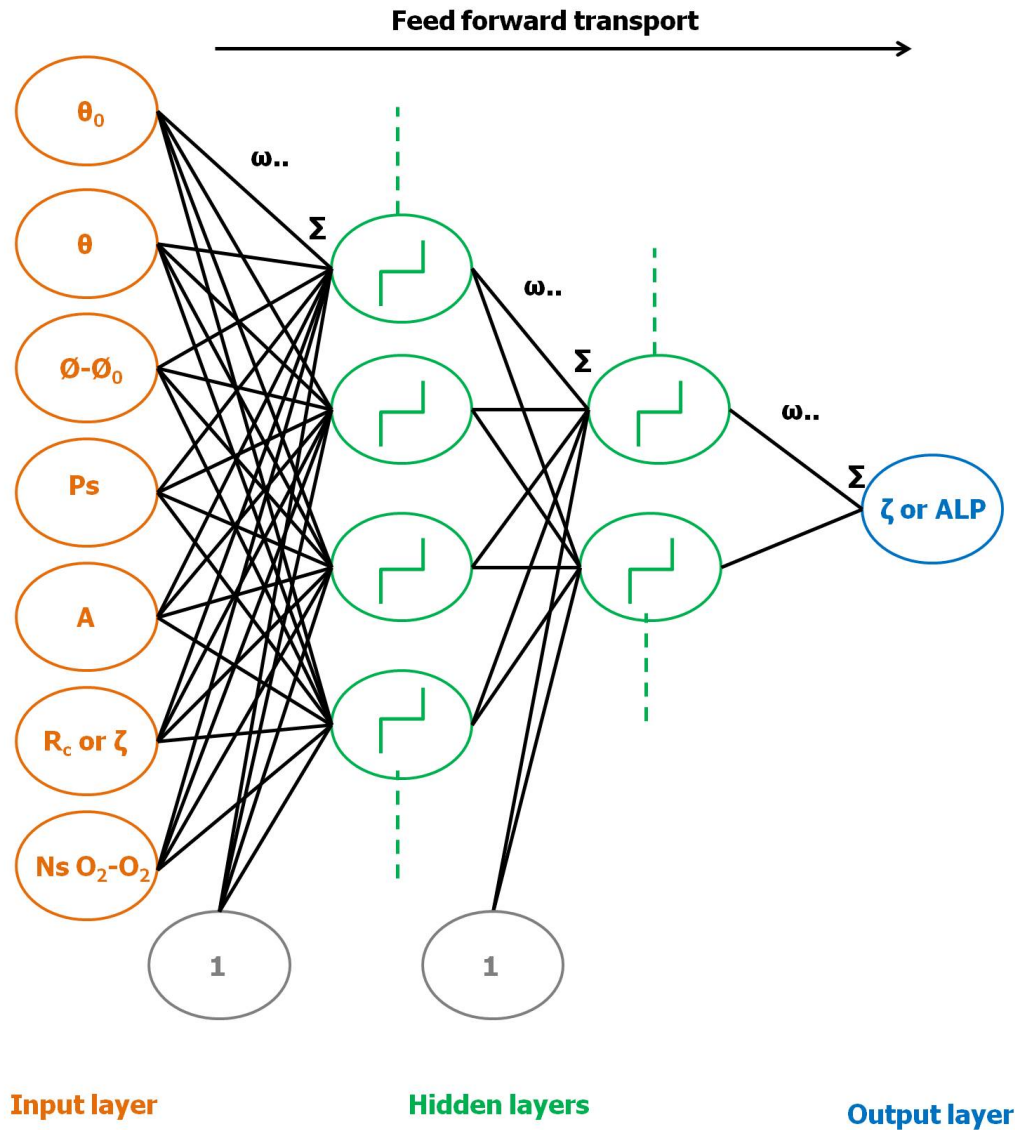


Figure 2. Diagram of Multilayer Perceptron (MLP) Neural Network (NN) architecture designed for Aerosol Layer Pressure (ALP) and aerosol optical thickness τ retrieval algorithms from the OMI O_2-O_2 spectral band at 477 nm. The input parameters are based on the list given in Table 1. The different considered approaches for the MLP design and their applications are more detailed in Sect. 3. Each circle represent a specific processor (named neuron) including either an input / output variable (in the input / output layer) or the activation function (i.e. sigmoid function in the hidden layer). The synaptic weights $\omega_{..}$ ensure the connections of neurons between two consecutive layers. A weighted sum Σ is performed before the transport through the activation function. Note the presence of the bias neurons, prior to the activation functions in the hidden layers. For simplicity, bias neurons are commonly visualized as values added to each neuron in the input and hidden layers of a network, but in practice are treated in exactly the same manner as other weights: all biases are simply weights associated with vectors that lead from a single node whose location is outside of the main network and whose activation is always 1. While the synaptic weights essentially change the steepness of the activation functions, the bias neurons allow to modify the origin of these functions from 0 to positive or negative values.

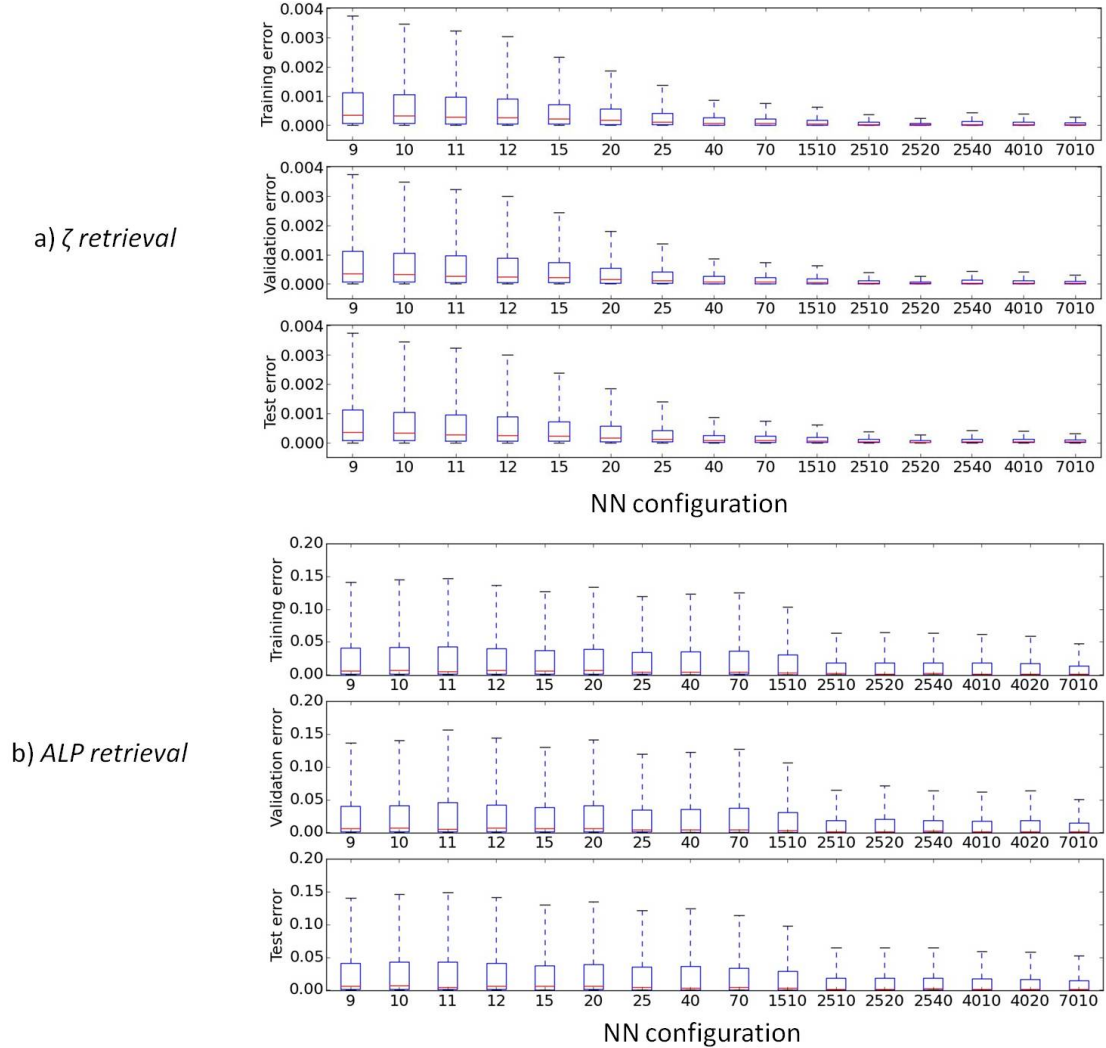


Figure 3. Box-whisker plots of the square of errors (see Eq. 7) obtained for different Neural Network (NN) configurations, at the end of their training, over the supervised data set (training-validation-test). The NNs XX have one hidden layer where XX indicate the number of neurons. The NNs YYXX have two hidden layers where YY and XX are the number of neurons in the 1st and 2nd hidden layer respectively: **(a)** NNs for τ retrieval, **(b)** NNs for ALP retrieval. Note that errors are computed over normalized output and true $\tau(550\text{nm})$ and ALP values (between -1 and 1) due to the definition of the sigmoid functions (see Sect. 3.1).

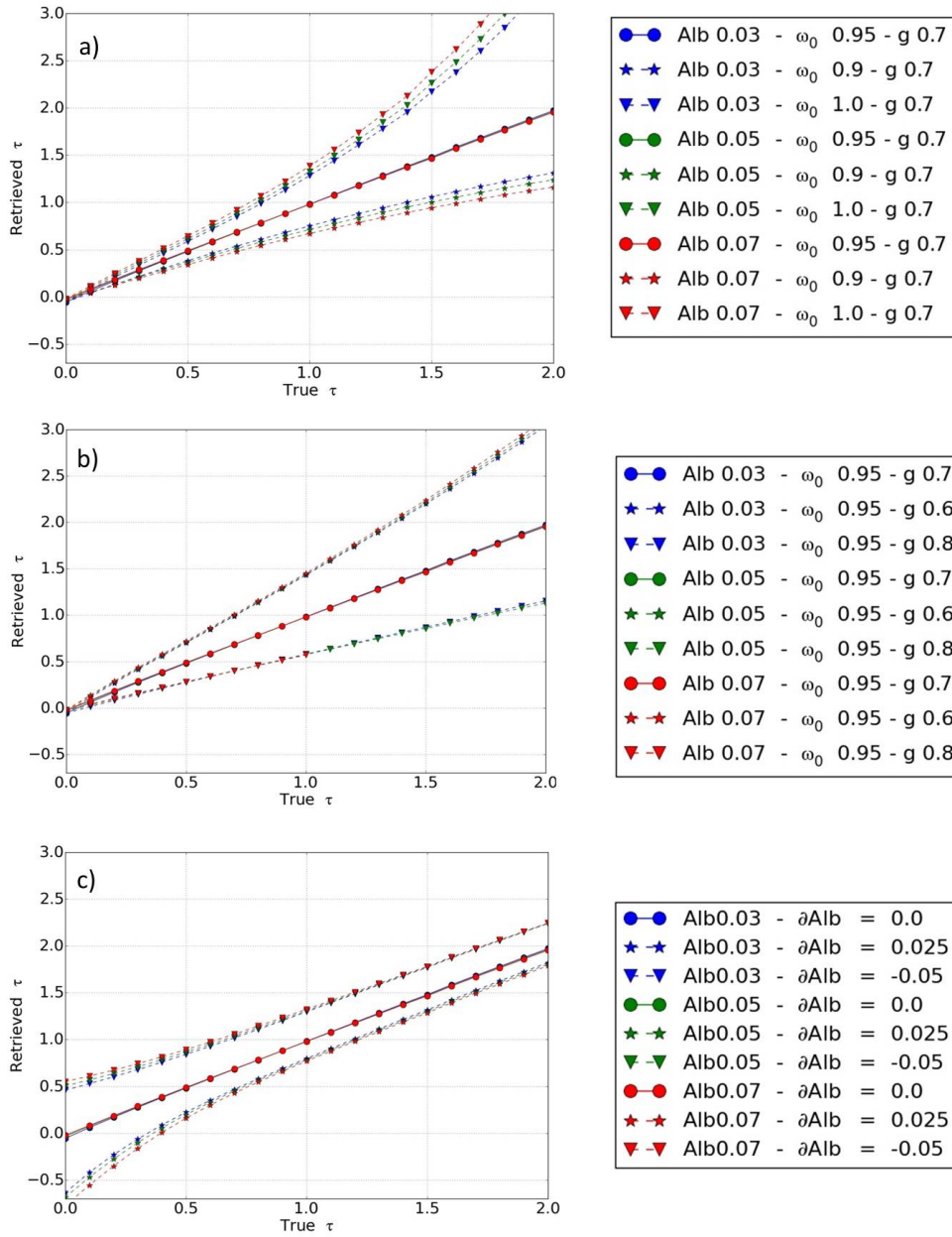


Figure 4. Simulated $\tau(550 \text{ nm})$ retrievals, based on noise-free synthetic spectra with aerosols, as a function of true $\tau(550 \text{ nm})$. The assumed geophysical conditions are: temperature, H_2O , O_3 , and NO_2 from climatology mid latitude summer, $\theta_0 = 25^\circ$ and $\theta = 25^\circ$, $P_s = 1010 \text{ hPa}$. All particles are located between 800 and 900 hPa and $\alpha = 1.5$. Note that the scenarios with lines and similar symbols general tend to fall on top of each other. The reference aerosol scenario is plotted with continuous lines and circle symbols and includes consistent aerosol optical properties with the supervision dataset used to train the neural network algorithm: i.e. $\omega_0 = 0.95$, $g = 0.7$. All the retrievals are achieved with the NN algorithm trained with $\omega_0 = 0.95$: **(a)** Sensitivity of $\tau(550 \text{ nm})$ retrievals to the aerosol single scattering albedo (true $\omega_0 = 0.95, 0.9$ or 1.0), **(b)** Sensitivity of $\tau(550 \text{ nm})$ retrievals to the aerosol asymmetry parameter (true $g = 0.6, 0.7$ or 0.8), **(c)** Sensitivity of $\tau(550 \text{ nm})$ retrievals to a surface albedo bias ($\partial \text{Alb} = 0.0, -0.025, 0.05$) with $\omega_0 = 0.95$, $g = 0.7$.

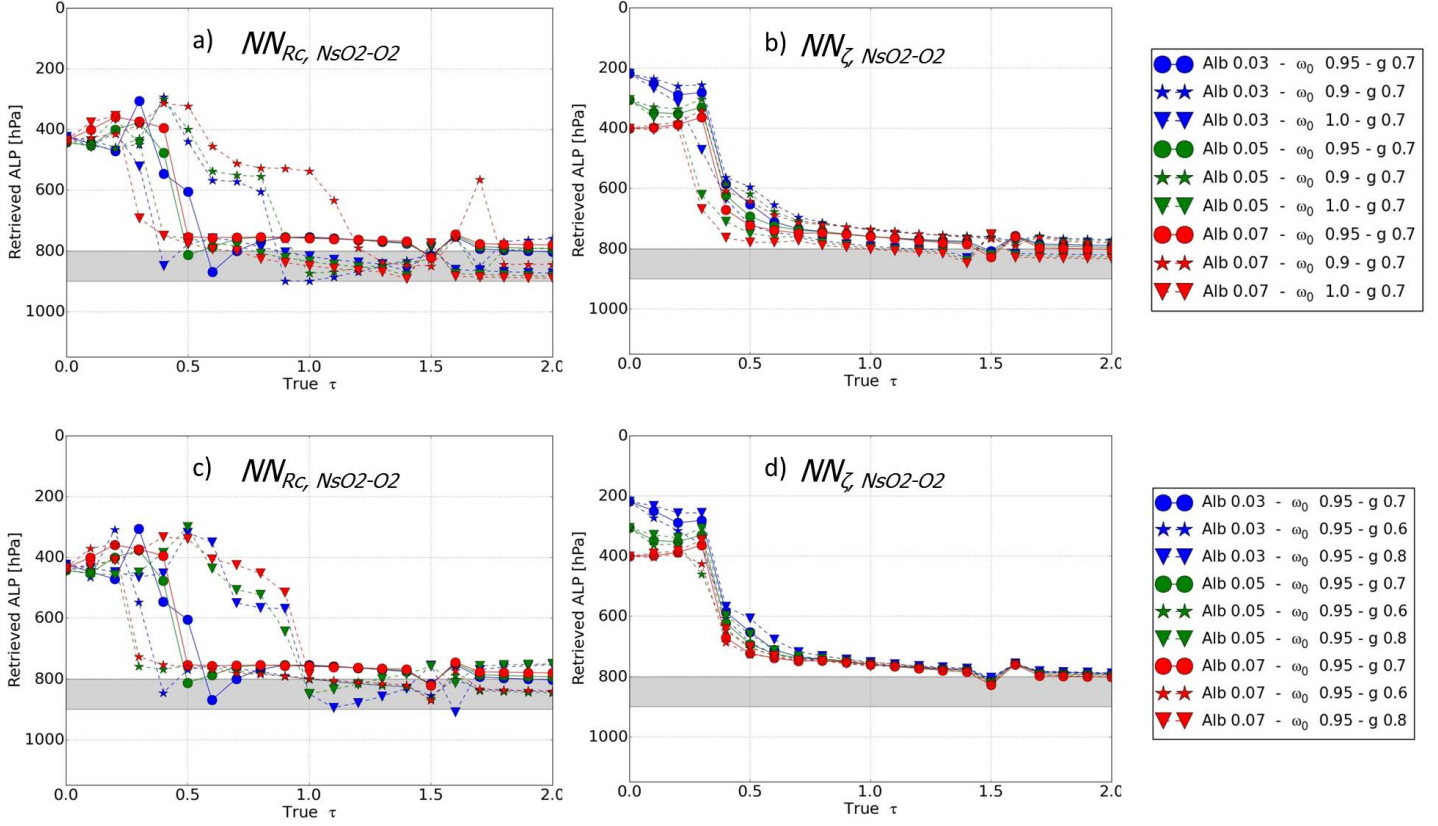


Figure 5. Simulated ALP retrievals, based on noise-free synthetic spectra with aerosols, as a function of true τ . All the retrievals are achieved with the two NN configurations ($NN_{R_c, N^s_{O_2-O_2}}$ and $NN_{\zeta, N^s_{O_2-O_2}}$) (see Sect. 3.1) trained with $\omega_0 = 0.95$. The assumed geophysical conditions are: temperature, H_2O , O_3 , and NO_2 from climatology mid latitude summer, $\theta_0 = 25^\circ$ and $\theta = 25^\circ$, $P_s = 1010$ hPa. The reference aerosol scenario assumes fine scattering particles ($\alpha = 1.5$, $\omega_0 = 0.95$, $g = 0.7$) located between 800 and 900 hPa: **(a)** and **(b)** Sensitivity of ALP retrievals to the aerosol single scattering albedo (true $\omega_0 = 0.95$ or 0.9) in the synthetic spectra, **(c)** **(d)** Sensitivity of ALP retrievals to the aerosol asymmetry parameter (true $g = 0.6, 0.7$ or 0.8) in the synthetic spectra.

Table 2. Summary of OMI $\tau(550\text{nm})$ and *ALP* retrieval error sources (either from $NN_{R_c, N_{\text{O}_2-\text{O}_2}^s}$ or from $NN_{\tau, N_{\text{O}_2-\text{O}_2}^s}$ combined with MODIS $\tau(550\text{nm})$) and budget as evaluated by the sensitivity analyses on synthetic data set (see Sect. 5) or on 3-year (2005-2007) observation measurements over North East-Asia (see Sect. 6)

Error source	$\tau(550\text{nm})$	From $NN_{R_c, N_{\text{O}_2-\text{O}_2}^s}$: <i>ALP</i> in [hPa] <i>ALH</i> in [m]	From $NN_{\tau, N_{\text{O}_2-\text{O}_2}^s}$ <i>ALP</i> in [hPa] <i>ALH</i> in [m]
$\tau(550\text{nm})$:			
True $\tau(550\text{nm}) \leq 0.5$ (see Sect. 5)	-	[250:400] [hPa]	[150:400] [hPa]
True $\tau(550\text{nm}) = [0.5 : 1.0]$ (see Sect. 5)	-	100 [hPa]	100 [hPa]
True $\tau(550\text{nm}) \geq 1.0$ (see Sect. 5)	-	≤ 50 [hPa]	≤ 50 [hPa]
MODIS $\tau(550\text{nm}) \geq 1.0$ (see Sect. 6)	-	650-1140 [m]	260-800 [m]
$\partial\tau(550\text{nm}) = 0.25$ (see Sect. 5)	-	-	50 [hPa] (true $\tau = 0.6 - 1.0$)
	-	-	Almost zero (true $\tau \geq 1.0$)
Surface albedo:			
$\partial A = 0.05$ (see Sect. 5)	0.25-0.5	> 100 [hPa] (true $\tau = 0.5 - 1.0$) 0-50 [hPa] (true $\tau \geq 1.0$)	50-100 [hPa] (true $\tau = 0.5 - 1.0$)
OMLER vs. MODIS black sky (see Sect. 6)	0.05-0.1	≤ 730 [m] (MODIS ($\tau \geq 1.0$))	≤ 180 [m] (MODIS ($\tau \geq 1.0$))
Aerosol Single Scattering Albedo ($\partial\omega_0 = 0.05$)			
(see Sect. 5)	0.8 (true $\tau = 2$) 0.1 (true $\tau = 0.5$)	> 100 [hPa] (true $\tau = 0.5 - 1.5$) 0-100 [hPa] (true $\tau \geq 1.0$)	0-50 [hPa] (true $\tau \geq 0.5$)
(see Sect. 6)	0.5 (MODIS $\tau = 1.5$)	540-1200 [m] (MODIS ($\tau \geq 1.0$))	560-660 [m] (MODIS $\tau \geq 1.0$)
Asymmetry parameter ($\partial g = 0.1$) (see Sect. 5)			
	0.5 (true $\tau = 1.5$) 0.25 (true $\tau = 0.5$)	200-400 [hPa] (true $\tau = 0.5 - 1.0$) 50 [hPa] (true $\tau \geq 1.0$)	0-50 [hPa] (true $\tau \geq 0.5$)
O_2-O_2 SCD ($\partial N_{\text{O}_2-\text{O}_2}^s$) (see Sect. 5):			
$\partial N_{\text{O}_2-\text{O}_2}^s = 0.05 \text{ mol}^2 \text{cm}^{-5}$	-	19 ± 29 [hPa]	19 ± 29 [hPa]
$\partial N_{\text{O}_2-\text{O}_2}^s = 0.25 \text{ mol}^2 \text{cm}^{-5}$	-	57 ± 31 [hPa]	57 ± 31 [hPa]
O_2-O_2 SCD temperature correction (see Sect. 6)	-	50-300 [m] (MODIS ($\tau \geq 1.0$))	50-300 [m] (MODIS $\tau \geq 1.0$)

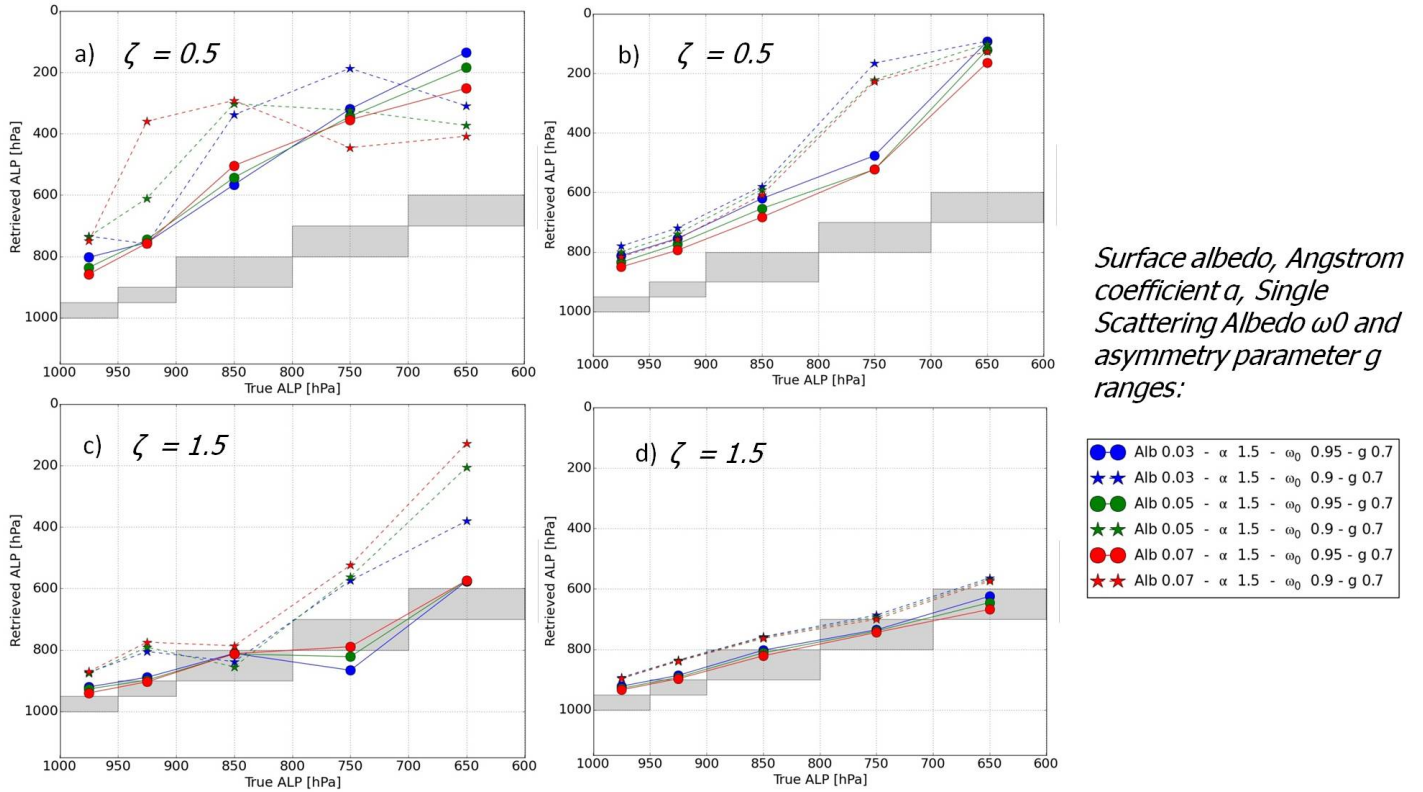


Figure 6. Simulated ALP retrievals vs. true ALP for 2 τ values (0.5 and 1.5) and the two NN configurations (see Sect. 3.1) and for the following conditions: temperature, H_2O , O_3 , and NO_2 from climatology mid latitude summer, $\theta_0 = 25^\circ$, $\theta = 25^\circ$, surface pressure = 1010 hPa and fine scattering aerosol particles ($\alpha = 1.5$, $\omega_0 = 0.95$, $g = 0.7$): (a) $NN_{R_c, N_{O_2-O_2}^s}$ and $\tau(550nm) = 0.5$, (b) $NN_{\tau, N_{O_2-O_2}^s}$ with true $\tau(550nm)$ value as input and $\tau(550nm) = 0.5$, (c) $NN_{R_c, N_{O_2-O_2}^s}$ and $\tau(550nm) = 1.5$, (d) $NN_{\tau, N_{O_2-O_2}^s}$ with true $\tau(550nm)$ value as input and $\tau(550nm) = 1.5$

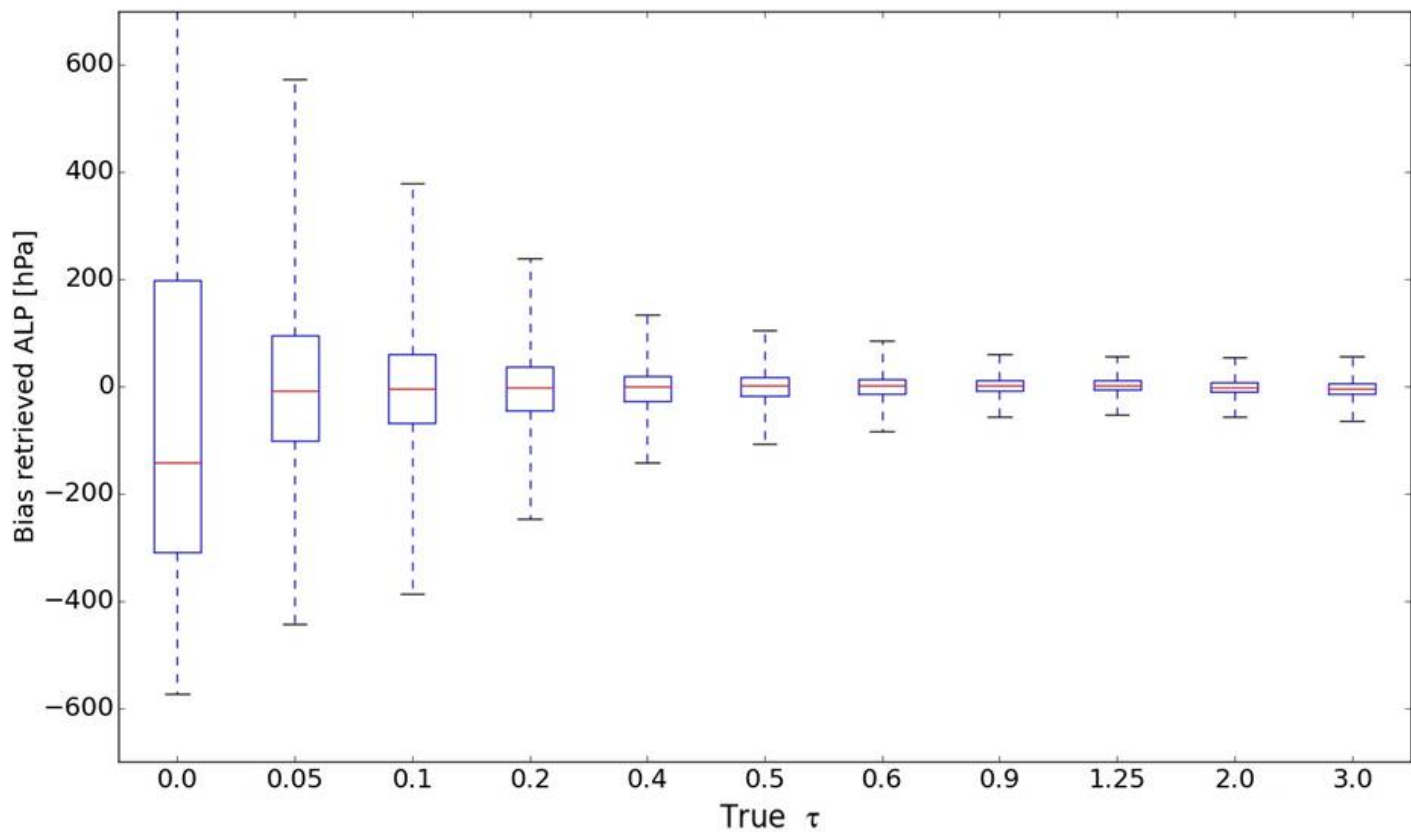


Figure 7. Box-whisker plots of retrieved Aerosol Layer Pressure (ALP) biases as a function of true τ (550nm) from $NN_{R_c, N_{O_2-O_2}^s}$ configuration over the the whole learning data set

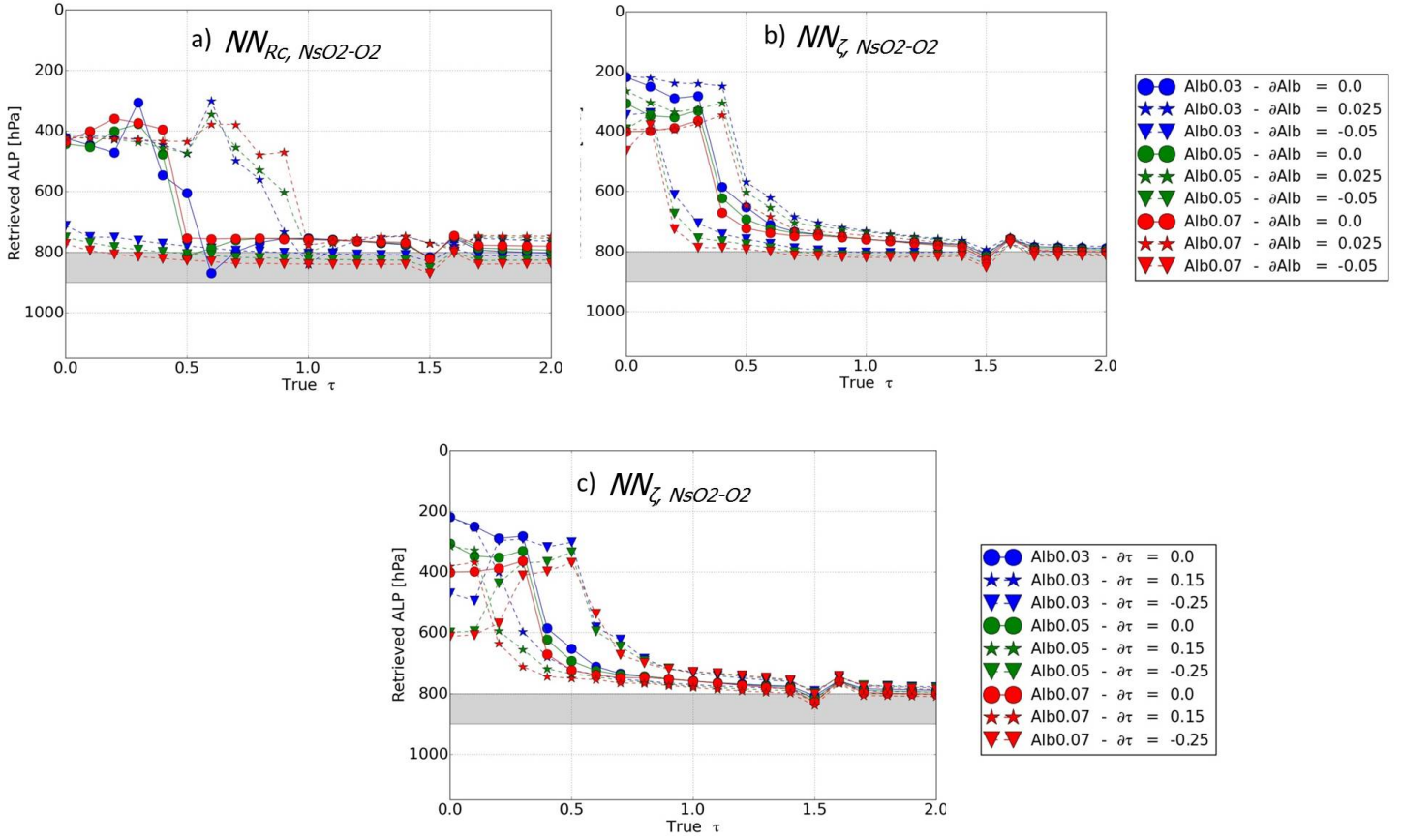


Figure 8. Simulated ALP retrievals, based on noise-free synthetic spectra with aerosols, as a function of true τ . The retrievals are achieved with the NN configurations (NN_{R_c, NsO_2-O_2} and / or NN_{τ, NsO_2-O_2}) (see Sect. 3.1) trained with $\omega_0 = 0.95$. The assumed geophysical conditions are: temperature, H_2O , O_3 , and NO_2 from climatology mid latitude summer, $\theta_0 = 25^\circ$ and $\theta = 25^\circ$, $P_s = 1010$ hPa. The reference aerosol scenario assumes fine scattering particles ($\alpha = 1.5$, $\omega_0 = 0.95$, $g = 0.7$) located between 800 and 900 hPa: (a) and (b) Sensitivity of ALP retrievals to a surface albedo bias ($\partial Alb = 0.0, -0.025, 0.05$) with NN_{R_c, NsO_2-O_2} and NN_{τ, NsO_2-O_2} , (c) Sensitivity of ALP retrievals to a $\tau(550nm)$ bias ($\partial\tau(550nm) = 0.0, -0.025, 0.05$) with NN_{τ, NsO_2-O_2} .

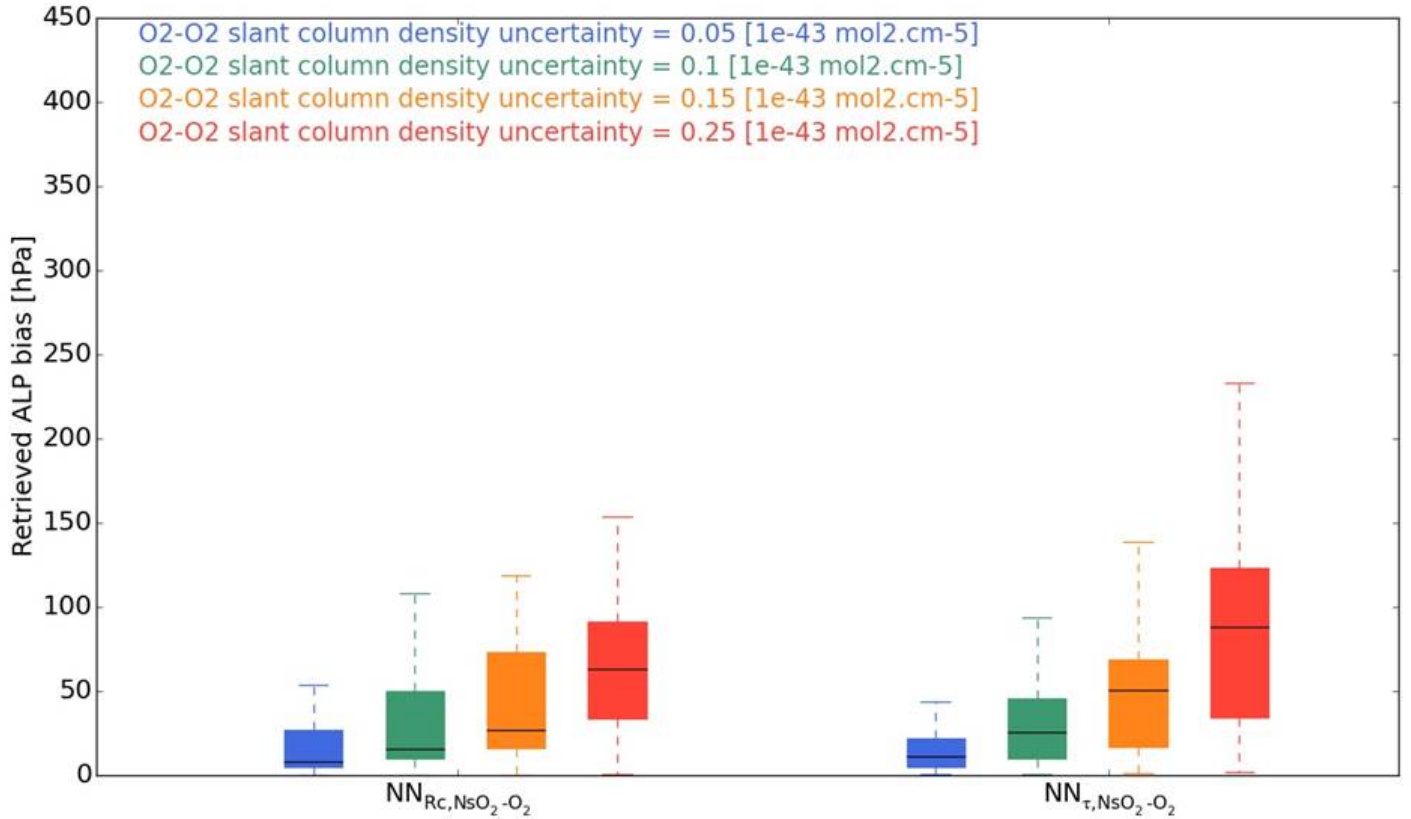


Figure 9. Box-whisker plots of ALP retrieval biases induced by O₂–O₂ SCD $N_{O_2-O_2}^S$ uncertainties. The assumed conditions are: fine scattering aerosols ($\alpha = 1.5$, $\omega_0 = 0.95$, $g = 0.7$), climatology mid-latitude summer temperature, NO₂, O₃ and H₂O profiles, surface pressure = 1010 hPa, surface albedo = [0.03-0.05-0.07] and combination of $\theta_0 - \theta = [25^\circ-25^\circ, 50^\circ-25^\circ, 25^\circ-45^\circ]$.

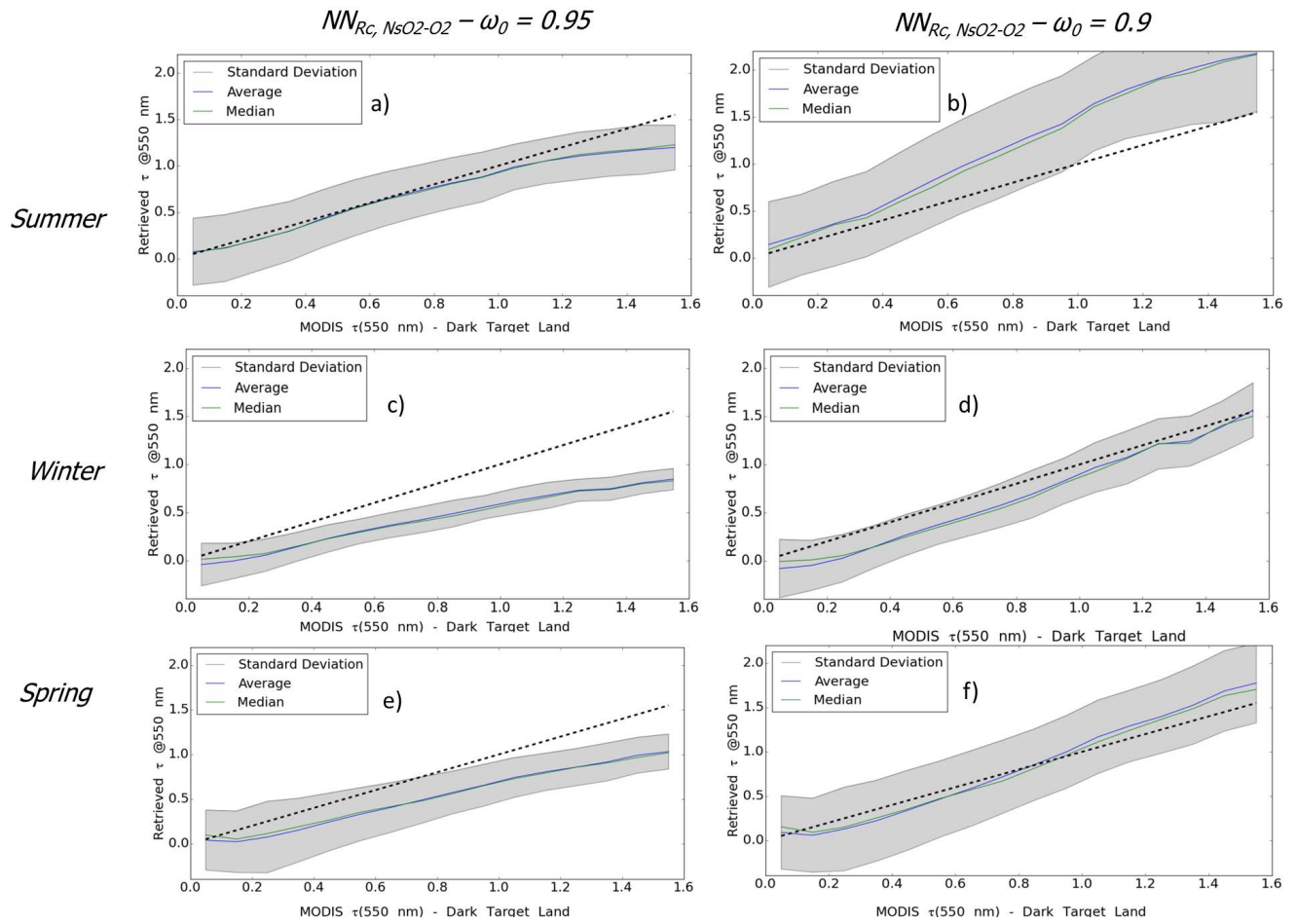


Figure 10. Collocated MODIS Aqua and retrieved OMI $\tau(550 \text{ nm})$ based on the OMLER surface albedo, over East China for cloud-free scenes and summer, winter and spring seasons. Statistics are computed over 3 years 2005-2007: (a), (c) and (d) assumed aerosol model with $\omega_0 = 0.95$, (b), (d) and (f) assumed aerosol model with $\omega_0 = 0.9$.

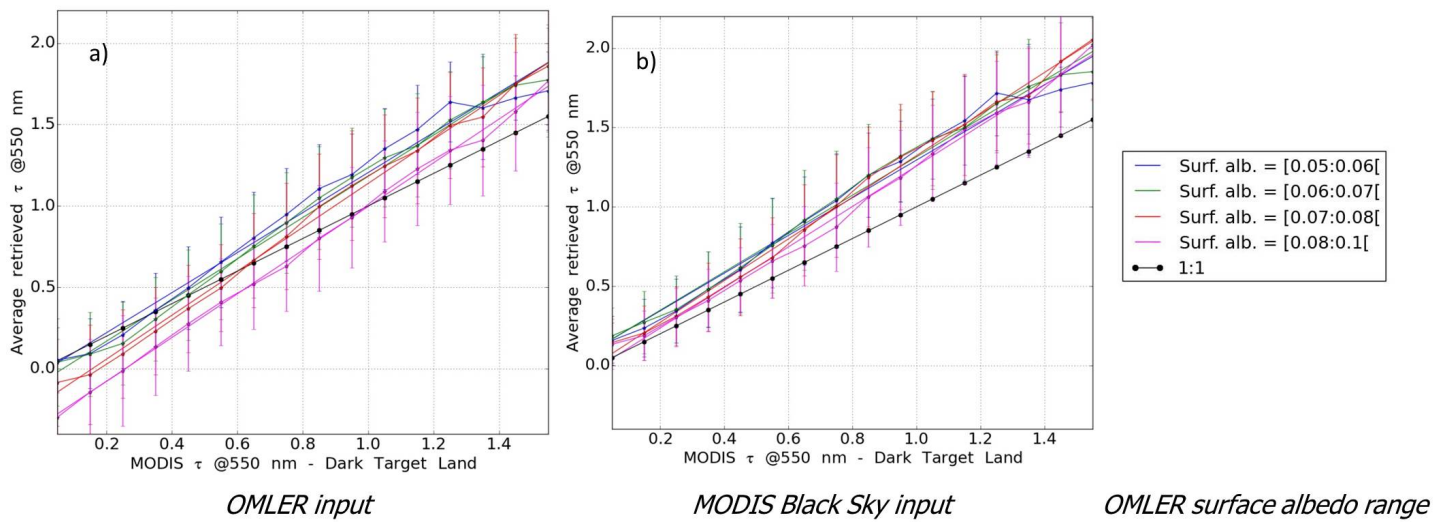


Figure 11. Collocated retrieved OMI retrieval and MODIS Aqua $\tau(550\text{nm})$ from Dark Target algorithm over land, over North-East Asia for cloud-free scenes in autumn season. Retrievals are depicted as a function of OMLER surface albedo ranges (Kleipool et al., 2008) (see Sect. 5.1). The dotted black line is the reference 1:1. Statistics are computed over 3 years 2005-2007: **(a)** OMI retrievals based on OMLER, **(b)** OMI retrievals based on MODIS Black Sky surface albedo.

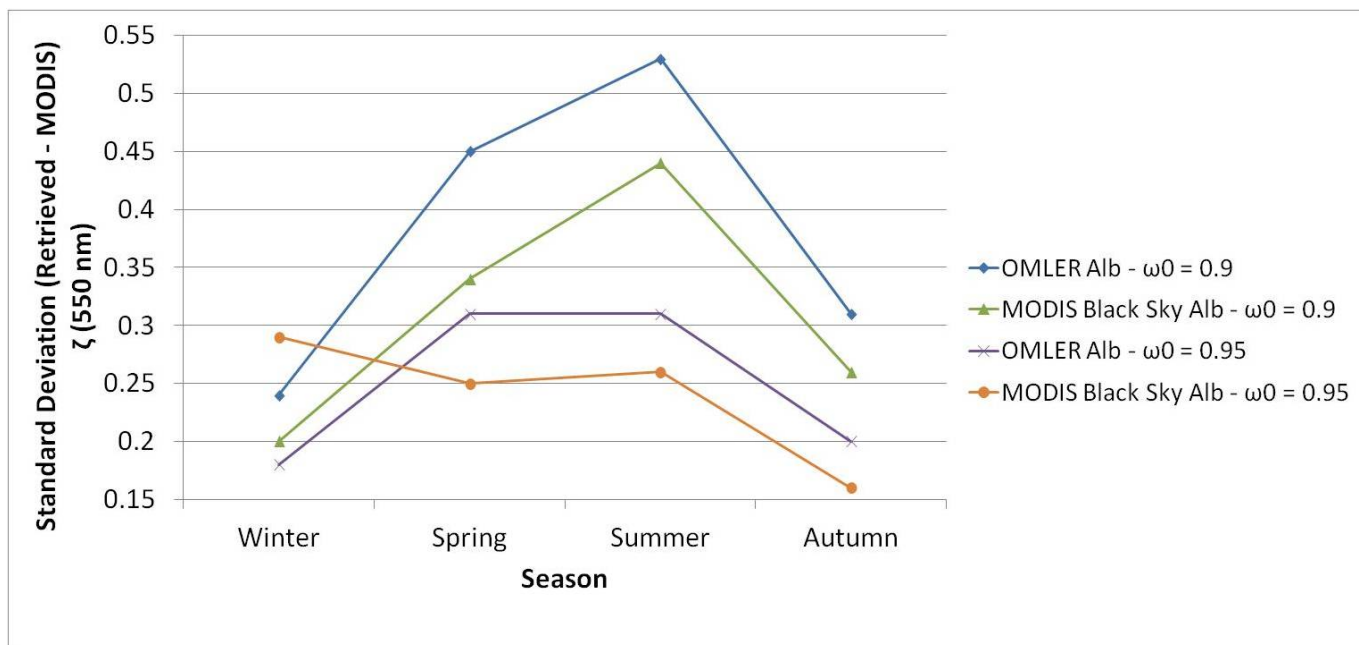


Figure 12. Standard deviation of the differences between OMI $\tau(550\text{nm})$ retrievals and MODIS $\tau(550\text{nm})$ from Dark Target Land algorithm over land for all the individual cloud-free observations over North-East Asia. The retrievals are obtained over 3 years 2005-2007, and for the 4 seasons. Aerosol single scattering albedo $\omega_0 = 0.95$ and $\omega_0 = 0.9$ are assumed. OMLER and MODIS Black Sky surface albedo are alternatively considered.

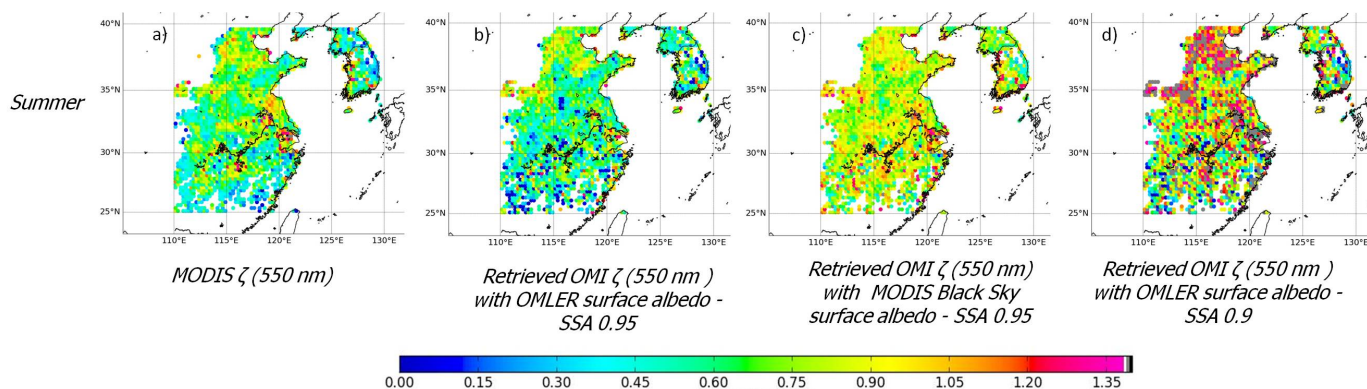


Figure 13. Spatial averages of $\tau(550\text{ nm})$ values, over North-East Asia for cloud-free scene. Statistics are computed over 3 years 2005-2007 for summer.

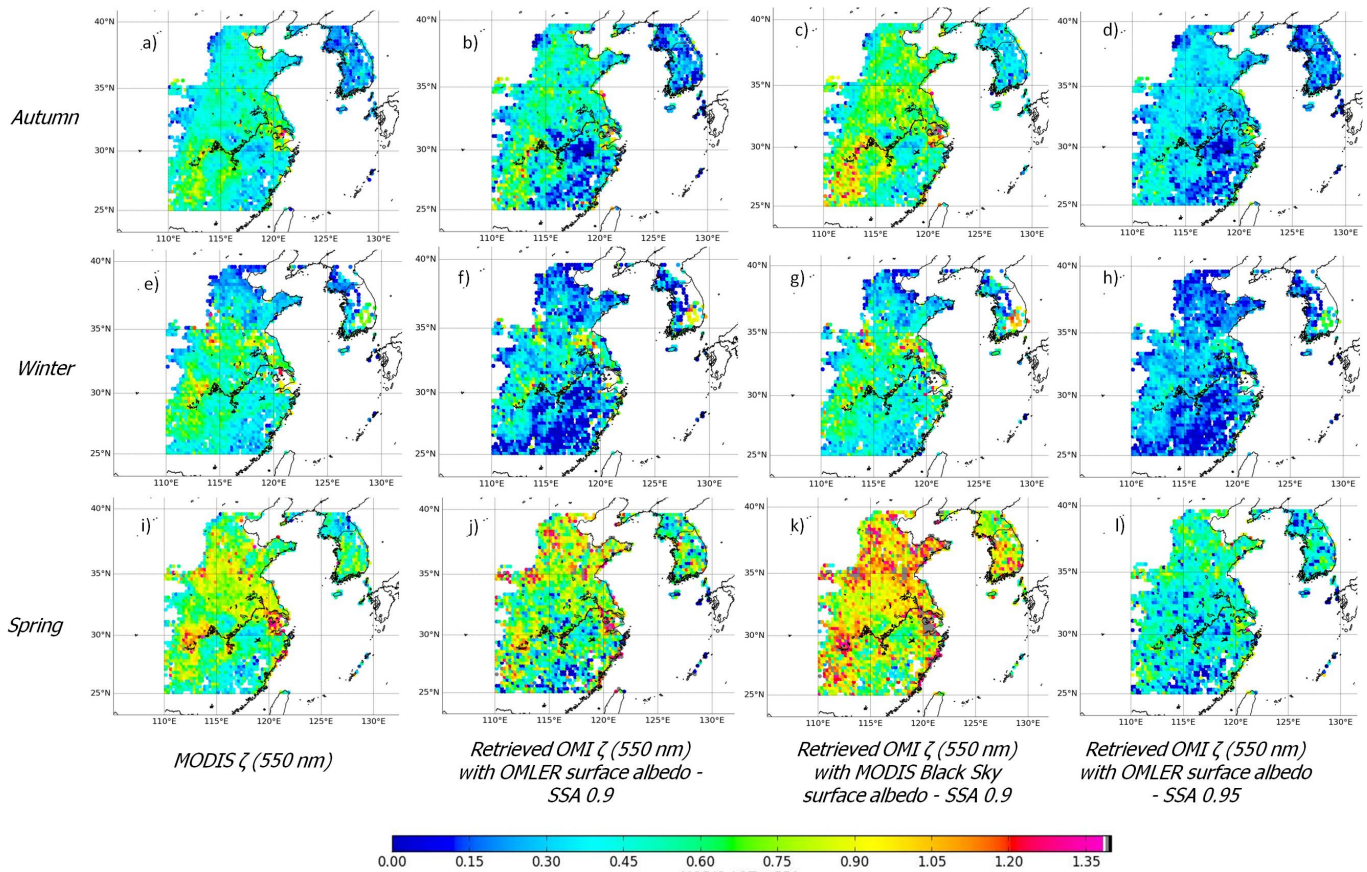


Figure 14. Spatial averages of $\tau(550 \text{ nm})$ values, over North-East Asia for cloud-free scene. Statistics are computed over 3 years 2005-2007 for the 3 seasons, autumn, winter and spring.

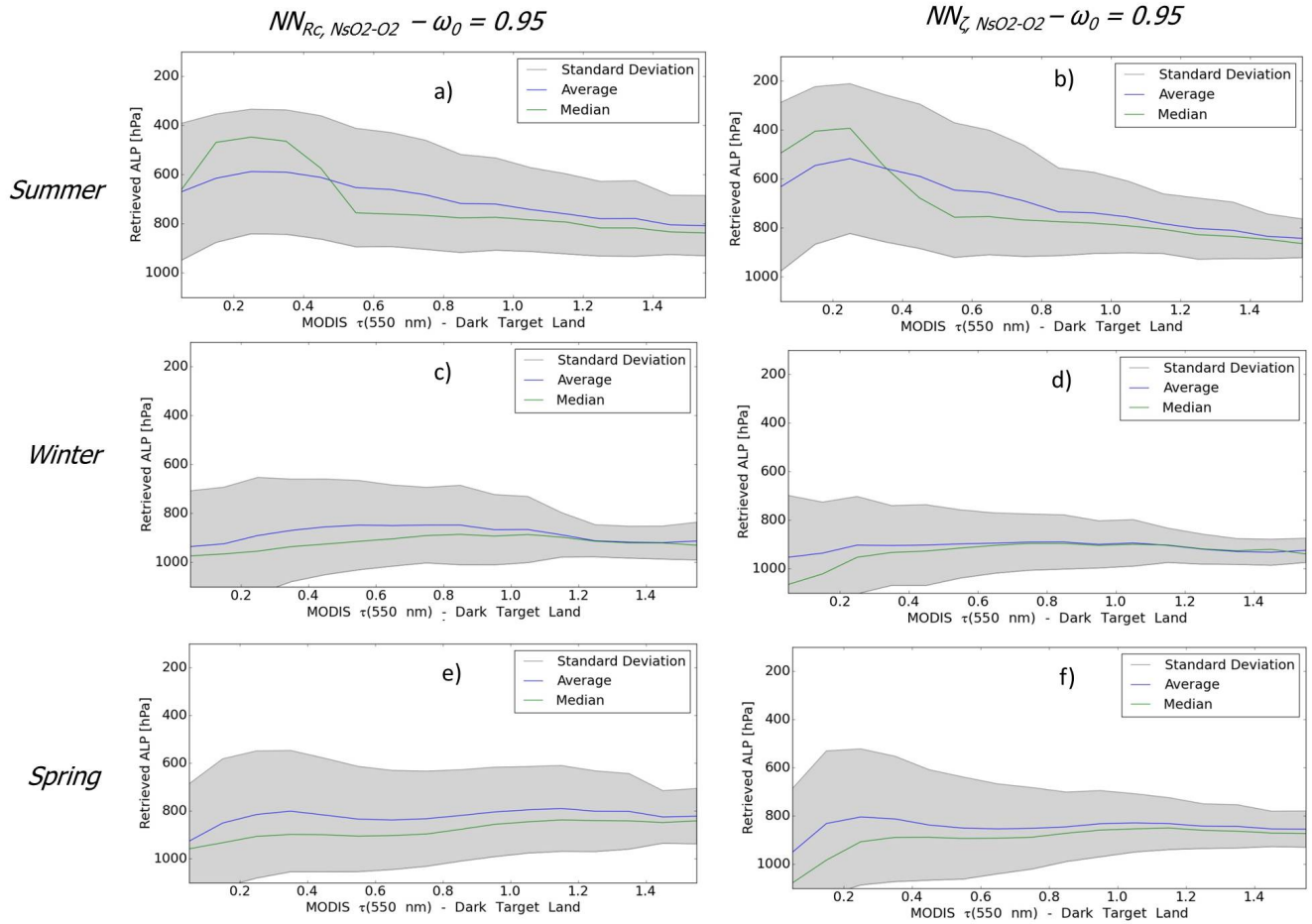


Figure 15. Collocated retrieved OMI ALP (assumed aerosol model with $\omega_0 = 0.95$ and based on the OMLER surface albedo) and MODIS Aqua $\tau(550 \text{ nm})$, over North-East Asia for cloud-free scenes and summer, winter and spring seasons. Statistics are computed over 3 years 2005-2007: (a), (b) and (c) OMI retrievals are from the NN_{R_c, NsO_2-O_2} configuration, (d), (e) and (f) OMI retrievals are from the NN_{τ, NsO_2-O_2} configuration with MODIS Aqua $\tau(550 \text{ nm})$, from Dark Target Land algorithm, as input (see Sect. 5.1).

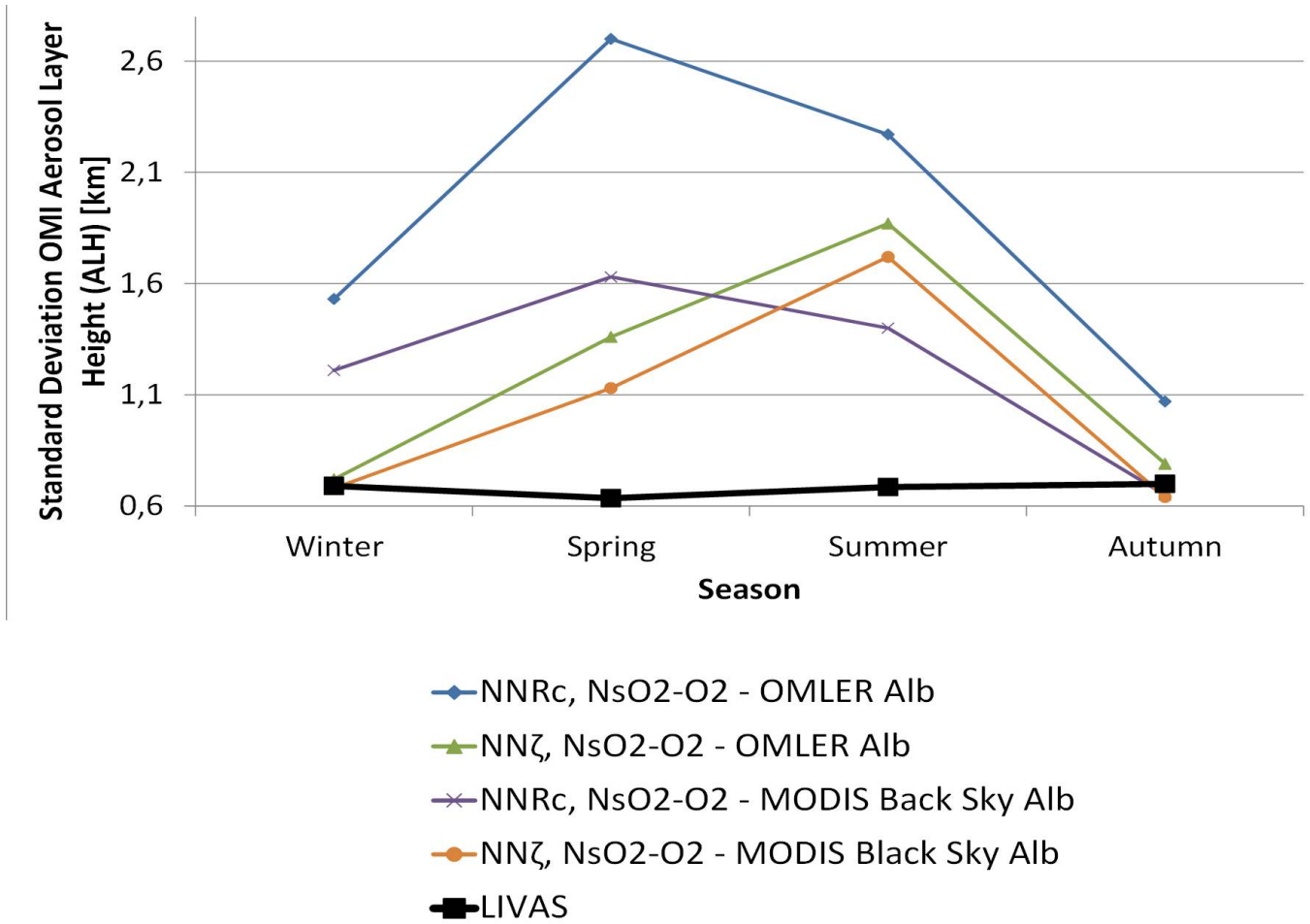


Figure 16. Standard deviation of the OMI ALH retrievals obtained for the cloud-free scenes with MODIS $\tau(550\text{nm}) \geq 1.0$ over North-East Asia. The retrievals are done for cloud-free scene, over 3 years 2005-2007. Aerosol single scattering albedo $\omega_0 = 0.95$ is assumed. OMLER and MODIS Black Sky surface albedo, and the NN configurations (NN_{Rc, NsO_2-O_2} and NN_{τ, NsO_2-O_2} with MODIS $\tau(550\text{ nm})$ as input) are alternatively considered (cf. Sect. 6.1).

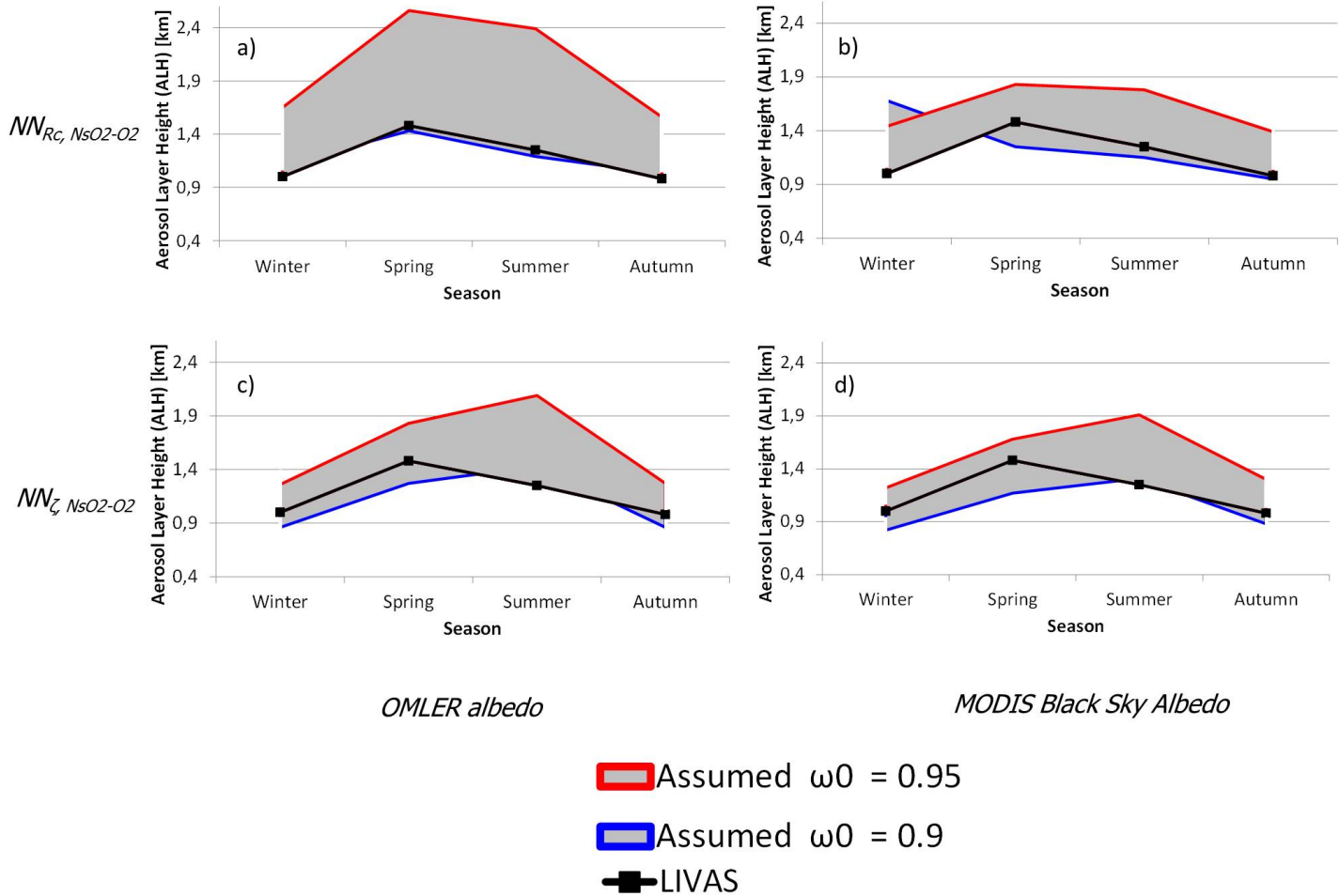


Figure 17. Comparison of the average of the OMI ALH retrievals obtained over scenes with collocated MODIS $\tau \geq 1.0$, with the LIVAS ALH climatology database. The retrievals are achieved over North-East Asia for cloud-free scenes, over 3 years 2005-2007, and for the 4 seasons. OMI and MODIS Black Sky surface albedos are alternatively considered. The 2 NN OMI ALH algorithms are used (see Sect. 5.1): $NN_{R_c, N_{O_2-O_2}}^s$ based on OMI $R_c(475 \text{ nm})$ and $NN_{\tau, N_{O_2-O_2}}^s$ based on MODIS $\tau(550 \text{ nm})$. A temperature correction is applied to the OMI $N_{O_2-O_2}^s$ prior to the retrievals (cf. Sect 6.1): **(a)** $NN_{R_c, N_{O_2-O_2}}^s$ algorithm and OMLER surface albedo, **(b)** $NN_{R_c, N_{O_2-O_2}}^s$ algorithm and MODIS Black Sky surface albedo, **(c)** $NN_{\tau, N_{O_2-O_2}}^s$ algorithm, and OMLER surface albedo, **(d)** $NN_{\tau, N_{O_2-O_2}}^s$ algorithm and MODIS Black Sky surface albedo.